X-ray Spectroscopic Studies of Gold-thiolate Nanoclusters

by

Mark A. MacDonald

Submitted in partial fulfillment of the requirements
for the degree of Master of Science

at

Dalhousie University
Halifax, Nova Scotia
May 2011

DALHOUSIE UNIVERSITY

DEPARTMENT OF CHEMISTRY

The undersigned hereby certify that they have read and recommend to the Faculty of Graduate Studies for acceptance a thesis entitled "X-ray Spectroscopic Studies of Gold-thiolate Nanoclusters" by Mark A. MacDonald in partial fulfillment of the requirements for the degree of Master of Science.

Dated: May 27th, 2011

Supervisor: _____

Readers: _____

_____

_____

Departmental Representative: _____

DALHOUSIE UNIVERSITY

DATE: May 27th, 2011

AUTHOR: Mark A. MacDonald

TITLE: X-ray Spectroscopic Studies of Gold-thiolate Nanoclusters

DEPARTMENT OR SCHOOL: Department of Chemistry

DEGREE: MSc CONVOCATION: October YEAR: 2011

_____

Signature of Author

I would like to dedicate this work to the members of the Zhang research group (Dan, Paul, Steve and Zac) for the camaraderie that made this experience feel more like play, than work. Good luck, guys.

TABLE OF CONTENTS

LIST OF TABLES

LIST OF FIGURES

ABSTRACT

Structural characterization of nanomaterials represents one of the largest challenges in modern nanoscience. Recent advances in the synthesis and crystallography of gold-thiolate nanoclusters have led to enormous progress in understanding the properties of these materials, however, many questions still exist about how the structure and bonding of these nanoclusters vary with cluster size, composition and material phase. The precisely defined size and composition of gold-thiolate nanoclusters offers a great opportunity to systematically illustrate the structure and bonding of these materials from an atomic-site-specific perspective.

Towards this end, X-ray absorption and photoemission spectroscopies were employed in the study of compositionally precise gold-thiolate nanoclusters. First, a high-precision, site-specific illustration of the bonding in a 144 Au atom nanocluster is presented. Following this, a comparison of the structure of a 38 Au atom nanocluster in the solid state and solution-phase is presented and discussed in terms of local structural and electronic effects. Finally, the structural changes experienced by a 25 Au atom nanocluster in response to temperature and solvation are observed from a site-specific perspective. In addition, size-specific bonding trends for these clusters are presented from both the sulfur and gold perspectives.

This work represents the first X-ray absorption spectroscopy study of compositionally precise gold-thiolate nanomaterials. These studies help to develop a thorough picture of the bonding properties of gold thiolate nanoclusters, and have potential implications for the development and application of gold-thiolate nanomaterials.

LIST OF ABBREVIATIONS USED

Au_{25}	$[N((CH_2)_7CH_3)_4]^{+1}$ $[Au_{25}(SCH_2CH_2Ph)_{18}]^{-1}$
Au_{38}	$Au_{38}(SCH_2CH_2Ph)_{24}$
Au_{144}	$Au_{144}(SCH_2CH_2Ph)_{60}$
BCC	Body-Centered Cubic
CLS	Canadian Light Source
CN	Coordination Number
DOS	Density of States
EXAFS	Extended X-ray Absorption Fine Structure
FCC	Face-Centered Cubic
FT	Fourier Transform
HXMA	Hard X-ray Microanalysis
l-DOS	Local Angular Momentum Density of States
MBA	4-Mercaptobenzoic Acid
NEXAFS	Near-Edge X-ray Absorption Fine Structure
NP	Nanoparticle
SGM	Spherical Grating Monochromator
SPR	Surface Plasmon Resonance
SR/HSR	Generic Thiolate Molecule
SXRMB	Soft X-ray Microcharacterization Beamline
UPS	Ultraviolet Photoelectron Spectroscopy
VLS-PGM	Variable-Line Spacing Planar Grating Monochromator
XANES	X-ray Absorption Near-Edge Structure

XAS	X-ray Absorption Spectroscopy
XPS	X-ray Photoelectron Spectroscopy

ACKNOWLEDGEMENTS

I would first and foremost like to thank the support and guidance of my supervisor, Dr. Peng Zhang throughout this work. As well, sincere thanks are extended to my supervisory committee (Dr. M. A. White, Dr. N. Schepp) and all the collaborators (Dr. R. Jin, H. Qian), beamline scientists (Drs. R. Gordon, N. Chen, Y. Hu, L. Zuin, T. Regier, and R. Blyth), technical staff (Dr. Z. Bayindir) and professors (Dr. H. Andreas, J. W. Zwanziger) who have aided my progress through the course of this work.

CHAPTER 1: INTRODUCTION

1.1 Nanomaterials:

Nanoscience is the study of materials with at least one dimension that falls within the nano-scale (~1-100 nm). These materials are of interest due to the new physicochemical properties that emerge from these nano-sized materials when compared to their bulk counterparts.[1] In particular the size dependence and tunability of properties such as electrical conductivity, optical absorption/emission, catalytic reactivity and magnetism have been the subject of intense research in the field of nanoscience.[2] In general these new, or enhanced, physicochemical properties can be rationalized by considering the effect of size reduction on the collective and local electronic properties of these materials.

A common collective electronic phenomenon observed for noble metal (e.g. Ag, Au) nanoparticles is the emergence of a strong peak in their optical absorption spectra commonly referred to as a surface plasmon resonance (SPR). The SPR of these noble metal nanoparticles can be explained by Mie theory which describes the phenomenon as a collective oscillation of the conduction electrons (i.e. the 6s electrons in Au) within the confines of the nanoparticle's surface.[3] As a result, the energy required for resonance of these oscillations becomes strongly dependent on particle size, morphology (spherical, rod shaped, core/shell etc...) and surface interface (solvent, protecting ligand). A second property which can be described as a collective electronic effect is superparamagnetism in iron oxide nanoparticles. The rationale for this observation is rooted in the idea that the iron nanoparticles are similar in size to an individual magnetic domain in the bulk

material. As a result, when these domain-sized particles are suspended in solution they can quickly organize and disorganize in the presence and absence of a magnetic field.[4] This leads to a material that is quickly magnetized and then demagnetized at room temperature. These collective electronic properties are not new to these nanomaterials, but rather become enhanced when the materials are isolated as nano-sized particles. These size dependent collective electronic properties can thus be tailored through the development of synthetic methods which control the size of the product nanomaterials.

Other applications of nanomaterials focus upon local electronic properties related to the atomic structure of the material. It has been observed that by reducing the dimensions of metal nanoparticles their ability to catalyze certain chemical and electrochemical reactions increases.[5-8] It is thought that the high population of these low coordinate surface sites (due to the high surface-area to volume ratio of the materials) is responsible for the increased activity. This is akin to the observation of a chemical reaction occurring faster at a defect site on a metal surface.

1.2 Gold Nanoparticles

Gold nanoparticles represent one of the most thoroughly studied classes of nanomaterials in the current literature.[2,9,10] While the history of gold nanoparticles dates back to the middle ages,[2] the most significant advance in modern nanoscience came in 1994 with the development of a simple two-phase procedure for synthesizing thiolate-stabilized gold nanoparticles by Brust et al.[11] The stability of the gold-thiolate bond allowed for the product nanoparticles to be dried, stored and re-dispersed as desired without any degradation or agglomeration of the product. In addition, the use of thiol-based ligands (of the form HS-R, where R represents an organic molecular tail) in the

synthesis of nanoparticles led to drastically improved control of the size and size distributions of the product nanoparticles and greatly facilitated functionalization of the product nanoparticles through variation of the ligand tail.[12,13] Following the establishment of the Brust synthesis was a period of explosive growth in both research interest and novel applications of gold nanoparticles in fields such as biosensors,[14] drug delivery[15] and imaging.[16] Today the Brust synthesis (or some modification thereof) remains the preeminent method of gold-thiolate nanoparticle synthesis with modern techniques allowing for careful control of the size, shape and properties of the product nanoparticles.

1.2.1 Gold-thiolate Nanoclusters

In the early 2000s it was observed that when attempting to synthesize extremely small gold-thiolate nanoparticles (diameter < 2 nm) the size dispersion of the nanoparticles becomes discrete, and only clusters of the formula $Au_m(SR)_n$ with particular values of (m, n) are thermodynamically stable synthetic products.[17,18] These small nanoparticles, commonly referred to as nanoclusters, are distinguishable from larger gold-thiolate nanoparticles due to their different physical and chemical properties.[19] In particular, the atomic packing symmetry of these small clusters does not match that of larger Face-Centered-Cubic (FCC) gold nanoparticles[20] and the optical spectra of these nanoclusters are no longer dominated by collective many electron excitations (i.e. SPR), but rather contain discrete single electron transitions between occupied and unoccupied electronic energy levels.[21] Due to these divergent properties, gold-thiolate nanoclusters have become established as a subclass of gold-thiolate nanoparticles and serve as a link between larger gold thiolate nanocrystals and inorganic

gold-thiolate complexes. The selective stability of certain nanocluster stoichiometries has been exploited in modern synthetic methods so that a particular cluster may be synthesized and isolated in extremely high purity.[20,22-24]

1.2.2 Au_{102}

The high purity syntheses of gold nanoclusters facilitated the first crystallization and resulting total structure determination of a gold-thiolate nanomaterial in 2007 by Jadzinsky *et al*.[25] This came as a breakthrough in the nanoscience community because it shed important insight into the long debated mode of interaction between gold and sulfur in these materials. The structure revealed a 102-atom gold nanocluster consisting of a 79-atom gold core covered by 44 4-mercaptobenzoic acid (MBA) ligands which were connected via 23 bridging gold adatoms (Figure 1-1).

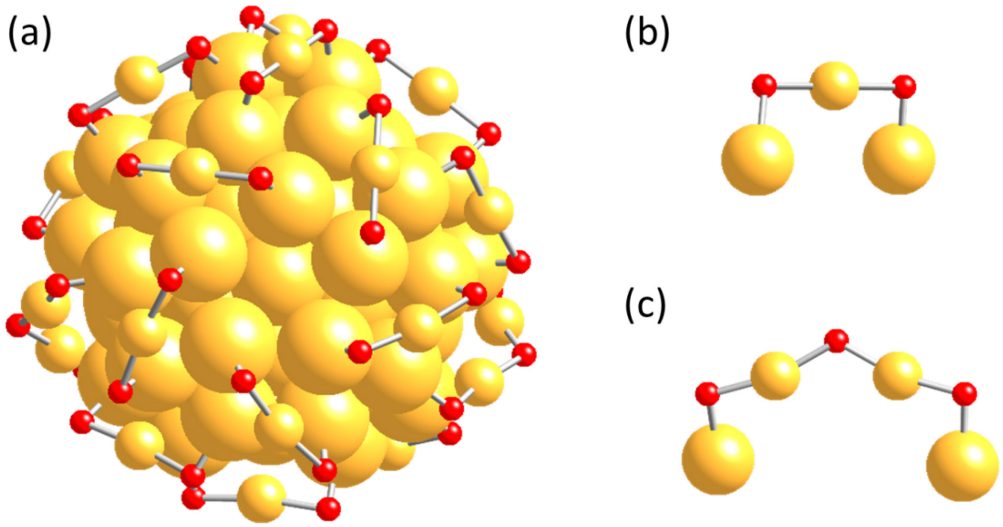

Figure 1-1: (a) Model of the $Au_{102}(MBA)_{44}$ nanoclusters. The (b) single and (c) double staple binding motifs are isolated for clarity, where yellow represents gold, and red represents sulfur atoms. The carbon tail of the sulfur ligand has been omitted for clarity.

This mode of surface passivation, commonly referred to as the staple motif (Figure 1-1, part b, c), was of interest for fundamental studies, as well as technical applications of these materials. How the staple motif can help to explain the exceptional stability of gold thiolate nanoclusters and how it may relate to larger gold-thiolate nanomaterials and self-assembled monolayers is a current field of research.[26,27]

Within the structure of Au_{102} three distinct Au bonding environments can be identified: core surface and staple. Core sites contain a high degree of Au-Au coordination (i.e. Au-Au coordination numbers of 10-12) and exist within the center of the nanocluster. Surface sites occur at the nanocluster surface and contain some Au-Au coordinations as well as one Au-S coordination anchoring the staple units to the cluster core. Staple sites contain two Au-S coordinations as well as long-range "aurophilic" Au-Au coordinations between the staple Au and the cluster core. As described by Schmidbauer,[28] the aurophilicity phenomenon is described as a super Van der Waals interaction that occurs between d^{10} Au systems (i.e. Au^{+}-Au^{+}). While the observation of long-range Au-Au interaction between surface and staple Au atoms in the Au_{25} and Au_{102} nanoclusters have been discussed in the literature, the description of the interaction as aurophilic may indeed be a misnomer and the long-range Au-Au interaction may be sufficiently described via traditional electron sharing/molecular orbital theory. This idea and how it applies to gold nanoclusters, however, requires further investigation.

1.2.3 Au_{144}, Au_{38} and Au_{25}

Throughout the present work a range of nanoclusters have been discussed, namely: $Au_{144}(SR)_{60,}$ $[TOA]^{+}[\ Au_{25}(SR)_{18}]^{-1}$ and $Au_{38}(SR)_{24}$ (where R = PhC_2H_4S- and TOA = tetraoctylammonium). For the sake of discussion these clusters, in addition to $Au_{102}(SR)_{44}$ will be identified simply by the number of Au atoms in their stoichiometry (i.e. Au_{25}, Au_{38}, Au_{102} and Au_{144}). For a detailed discussion of their structure and bonding please see Chapters 2, 3 and 4. Within this work the nanoclusters examined were prepared using phenylethanethiol as the capping ligand. Thus the trends and properties observed are unique to this system. A more rigorous study using various different ligands could provide a more comprehensive understanding of these materials.

The nanoclusters examined within this work were provided via collaboration with Huifeng Qian and Dr. Rongchao Jin at Carnigie Melon University in Pittsburgh, PA. All syntheses and characterization of the purity of these materials were conducted according to their previously published procedures for Au_{25},[22] Au_{38}[29] and Au_{144}.[20] All experiments within this work examined these materials as they were received.

1.3 X-ray Absorption Spectroscopy

Structural characterization of nanomaterials is one of the largest challenges in modern nanoscience. Due to the extremely small size of the materials, there is a natural breakdown of the long-range order which makes the information obtained from traditional structural characterization methods, such as powder X-ray diffraction, limited. As a result modern nanoscientists employ a range of techniques to characterize their materials such as electron microscopy, atomic force microscopy and electrochemical techniques. Towards this goal, X-ray spectroscopy (including both absorption and

photoemission spectroscopies) has emerged as an invaluable toolset for studying the structure and electronic properties of nanomaterials. In particular, when these tools are combined with *ab initio* calculations they can provide deep insight into the structure and bonding of nanomaterials.

X-ray absorption spectroscopy (XAS) measures the way in which an X-ray beam passing through a material is absorbed by a core level electron of an atom in the material.[30,31] Absorption of an X-ray by a core level electron will not occur until the incident photon carries sufficient energy to promote the electron into an unoccupied energy state above the Fermi level. As a result, a sharp attenuation of the X-ray beam, typically called an absorption edge, occurs when the incident photon energy is equivalent to the core level binding energy of the atom. The way in which the sample attenuates the X-ray beam provides information about the geometric and electronic environment around the nuclei under study. The quantity which describes this attenuation is called the X-ray absorption coefficient, μ, and is related to the measured X-ray beam intensity by the equation:

$$\mu(E) = \log(I_0/I) \qquad (1)$$

where I_o and I represent the intensity of the X-ray beam before and after transmission through the sample (Figure 1-2).

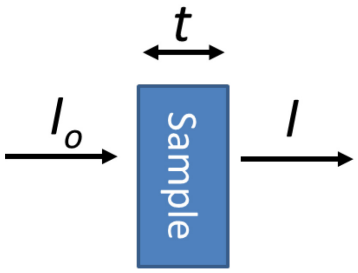

Figure 1-2: Schematic view of X-ray transmission through a material. I_o and I represent the intensity of the X-ray beam before and after transmission through the sample, respectively, while t represents the sample thickness.

Considering the X-ray absorption behavior of an isolated atom in a material, ignoring the influence of the local environment, a step-like attenuation of X-ray intensity, followed by a smooth decay, would be observed (Figure 1-3, part a). This interaction, called μ_0, is the normal interaction of an atom with X-rays, and is related to density, x-ray energy, atomic number and atomic mass (i.e. step-like absorption at core level binding energy followed by decay) rather than any structural parameters of the materials.[30,31] XAS studies how this absorption behavior changes due to the local environment of the atom under study (Figure 1-3, part b). This is achieved by analyzing the changes in the attenuation of μ, or the oscillations, of an X-ray absorption spectrum.

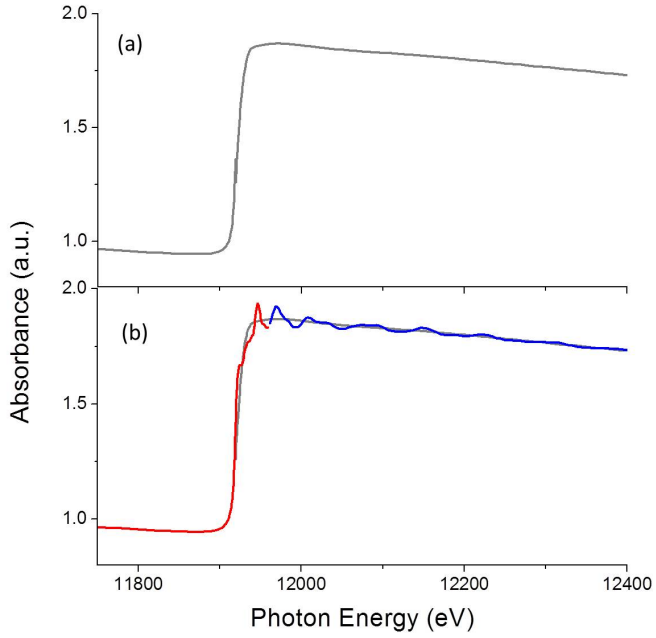

Figure 1-3: (a) The isolated atomic X-ray absorption, μ_0, and (b) real X-ray absorption coefficient, μ, of gold foil measure at the L_{III}-edge. The resulting changes in absorption in (b) can be attributed to the effect of neighboring gold atoms. In (b) the spectra has been divided into the near-edge (red) and extended (blue) regions of an X-ray absorption spectrum and overlaid on top of μ_0 (grey).

There are both benefits and challenges associated with conducting XAS experiments. The reliance of XAS on electronic excitation makes it accessible to any element with core level electrons and applicable to materials in any physical state (i.e. amorphous, liquid, etc...). However, in order to conduct an XAS experiment, a source of X-rays that is both tunable across a wide energy range and extremely bright is required. Thus, to conduct an XAS experiment a synchrotron X-ray source must be available. The anatomy of a XAS experiment can be broken into two main portions: Extended X-ray Absorption Fine Structure (EXAFS) and X-ray Absorption Near-Edge Structure (XANES).

1.3.1 Extended X-ray Absorption Fine Structure

Extended X-ray absorption fine structure, or EXAFS, represents the quantitative structural portion of an XAS experiment. In an EXAFS experiment the attenuation of X-rays in the region far past the absorption edge is observed (Figure 1-3, part b). This attenuation originates from the absorption of an X-ray photon by a core level electron which is subsequently ejected as a photoelectron wave (Figure 1-4).

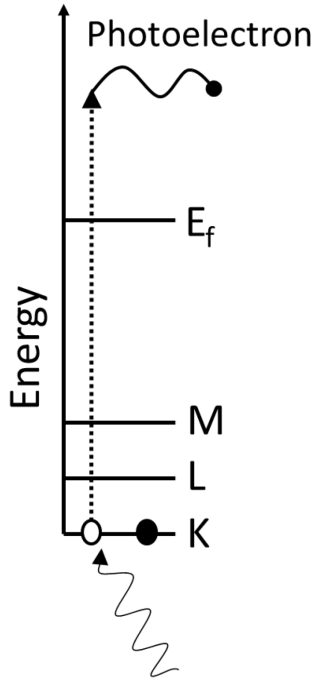

Figure 1-4: Schematic representing the underlying mechanism of EXAFS. A core level electron is excited by an incoming photon and ejected as a photoelectron.

The mechanism of EXAFS can be conceptually understood through several key steps (Figure 1-5). First, the photoelectron wave generated by X-ray absorption travels through the material, eventually reaching a neighboring atom. This wave then interacts with the neighboring atom's electron density, which causes the photoelectron wave to be scattered back towards the original absorbing atom. The resulting phase and amplitude of this

backscattered photoelectron depend upon the incident photon energy and the atomic number of the neighboring atom(s). Finally, this backscattered wave will add constructively or destructively to the original photoelectron wave as it returns to the original absorbing atom. When the backscattered wave is in phase with the original photoelectron wave the absorption of X-rays by the sample, and thus μ, is increased.[30-32] Likewise, if the backscattering is out of phase there will be an observed decrease of μ.

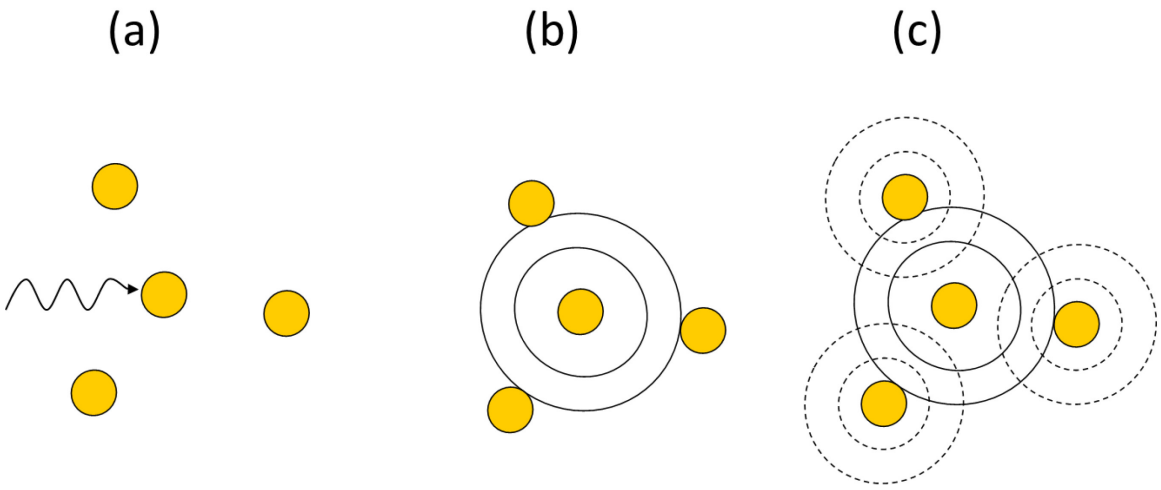

Figure 1-5: Schematic representation of the main mechanism behind the modulation of μ in the EXAFS region. The steps involved include (a) absorption of an X-ray photon and (b) ejection of a photoelectron wave and (c) backscattering of the photo electron wave off of neighboring atoms. The way in which the outgoing and backscattered photoelectron waves interfere causes the observed attenuation of X-rays in the EXAFS region of an XAS experiment.

The resulting fine structure, χ, is obtained from μ by:

$$\chi(E) = \frac{\mu(E) - \mu_0(E)}{\Delta\mu_0(E)} \qquad (2)$$

which is achieved by subtracting a background function to represent μ_0 and dividing by the "edge jump" or $\Delta\mu_0$ which represents the difference in X-ray attenuation before and

after the absorption edge. Customarily χ is displayed as a function of photoelectron wavenumber, $\chi(k)$, rather than energy, where:

$$k = \sqrt{\frac{2m(E-E_0)}{\hbar^2}} \tag{3}$$

and m is the electron mass, E the energy of the incoming photon, E_o the binding energy of the core level electron, and $\hbar$ the reduced Planck constant. The fine structure, $\chi(k)$ (often referred to as k-space), represents a superposition of all the scattering paths around the absorbing nuclei (Figure 1-6, part a). Due to the dependence of the backscattering amplitude on both energy and atomic number it is common to weight $\chi(k)$ by k^n, with n equal to 0, 1, 2 or 3, to make the amplitude of the spectrum more uniform. The $\chi(k)$ can then be treated by Fourier analysis and the components of $\chi(k)$ can be separated out based on distance from the absorbing atom, R, providing a radial bond distribution about the absorbing atom (Figure 1-6, part b).

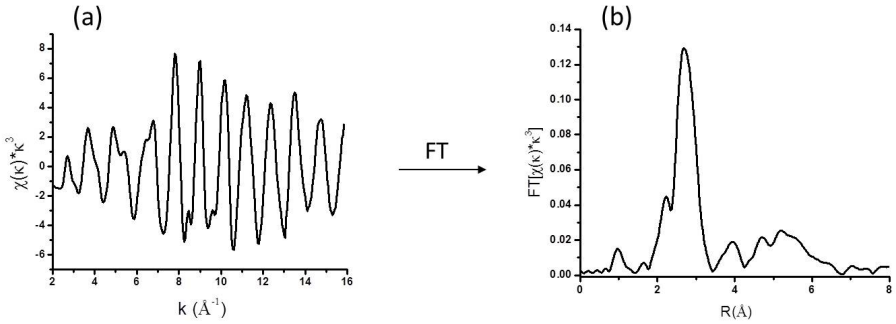

Figure 1-6: The (a) $\chi(k)*k^3$ and (b) FT[$\chi(k)*k^3$] obtained from XAS at the Au L_{III}-edge. By weighting the $\chi(k)$ by a factor of k^3 the oscillation amplitude is made more uniform across all values of k before Fourier transformation. The peaks in part (b) represent the radial bond distribution around the absorbing Au atom in Au foil, with the large peak at ~2.7Å representing the first Au-Au coordination shell.

The Fourier transformation of the $\chi(k)$ can then be refined to a structural model of the material which will yield structural information about the local bonding environment.

Refinement of an EXAFS spectrum is conducted by a least squares fitting method using the EXAFS equation, which for a single scattering interaction takes the form:

$$\chi(k) = \frac{N e^{-i k^2 \sigma^2} e^{-2R/\lambda(k)} f(k)}{kR^2} \sin[2kR + \delta(k)] \qquad (4)$$

where N represents the degeneracy of the scattering path, or coordination number, σ^2 represents the mean squared displacement of the scattering atom, λ represents the inelastic mean free path of the photoelectron, R represents the bond length and $f(k)$ and $\delta(k)$ represent the scattering amplitude and phase shift of the neighboring atom, respectively, and depend upon the photon energy and the atomic number of the neighboring atom.[30-32] For a real system with many scattering paths the EXAFS equation takes the form[32]:

$$\chi(k) = S_o^2 \sum_i \frac{N_j e^{-i k^2 \sigma_j^2} e^{-2R_j/\lambda(k)} f_j(k)}{kR_j^2} \sin[2kR_j + \delta_j(k)] \qquad (5)$$

where i represents a different coordination sphere (i.e. first nearest neighbor, second nearest neighbor, etc.), often called shells. In addition, a constant called the amplitude reduction factor (S_o^2) is introduced, which accounts for intrinsic losses in the X-ray absorption spectrum. During EXAFS refinement the threshold energy, E_o, is also allowed to vary in order to account for assumptions made during data workup and refinement. In order to refine an EXAFS spectrum and extract structural information (*N,*

R, σ^2) the scattering amplitude, and phase shift must be determined for the neighboring atom(s). Traditionally this was achieved by collecting the EXAFS spectrum of a well understood sample with a similar structure (i.e. foil, bulk material) and extracting the amplitude and phase from the experimental data. More commonly, however, these refinement standards are produced by *ab initio* simulations of structural models using the FEFF program code.[32] This produces high quality EXAFS fitting files which can be refined to fit the experimental data.

1.3.2 X-ray Absorption Near-Edge Structure

Typically, the XANES region of an XAS spectrum extends to approximately 40 eV past the absorption edge (core level binding energy). Within this region "near the edge" one can observe electronic transitions and multiple scattering photoelectric effects that can provide detail about the structure (lattice symmetry, coordinate environment) and electronic properties (oxidation state, band occupation) for the element in study.[30,31,33,34] Specifically, the transitions observed closest to the absorption typically represent transitions from occupied core states to unoccupied valence states (Figure 1-7, part a).

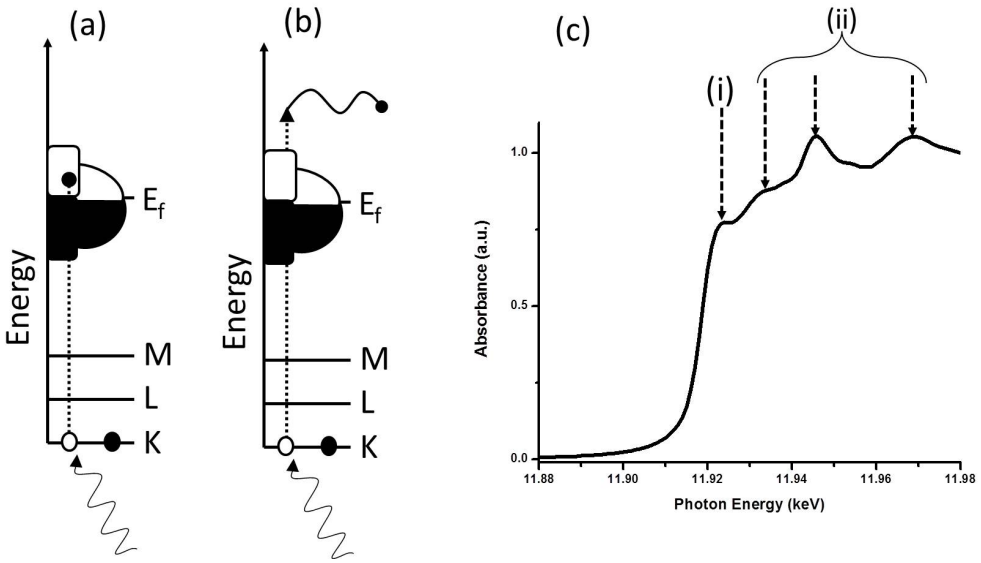

Figure 1-7: Schematic representing (a) the transition of a core electron into an unoccupied energy state and (b) emission of a photoelectron following X-ray absorption. The Fermi level is marked by E_F while the core levels are marked using XAS nomenclature. Part (c) represents the XANES region of an XAS scan of Au foil at the L_{III}-edge. Feature (i) represents transitions from the 2p level to unoccupied 5d-states while the three features marked by (ii) are the result of multiple scattering and when seen together are indicative of a face-centered cubic (FCC) lattice structure.

These transitions can sometimes be lower in energy than the normal binding energy of the core electron in which case they are called pre-edge features due to their occurrence before the normal absorption edge. Other features in a XANES spectra are associated with complex multiple scattering events that occur. This is attributed to the large mean-free path of the low energy (i.e. kinetic energy less that ~40 eV) photoelectrons created by the promotion of the core electron to the continuum level (Figure 1-7, part b).[32] As a result this photoelectron can scatter off multiple (i.e. two or more) atoms before returning to the original absorbing atom (Figure 1-8).

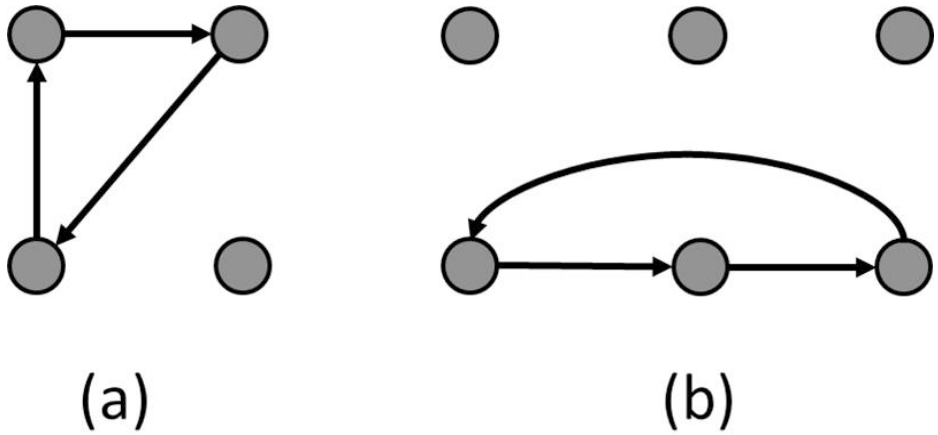

Figure 1-8: Illustration of some common multiple scattering paths taken by photoelectrons in XAS experiments. Both (a) triangular and (b) linear multiple scattering paths contribute significantly to the XANES, however, many other scattering paths are possible.

These multiple scattering events can provide a structural fingerprint for materials and provide qualitative information about the structure around the absorbing atom, such as the lattice type of a metal system (Figure 1-7, part c).

The transitions observed in a XANES spectrum are governed by quantum mechanical dipole selection rules whereby:

$$\Delta l = \pm 1 \tag{6}$$

where Δl represents the difference of the angular momentum quantum numbers of the final and initial electronic states. In both EXAFS and XANES the initial electronic states are described using XAS nomenclature (Table 1-1).

Table 1-1: A comparison of XAS nomenclature for electronic core level states, and the dipole-allowed final state symmetry of the transitions observed in the XANES region.

Edge	Initial State	Final State
K	1s	p
L_I	2s	p
L_{II}	$2p_{1/2}$	s, d
L_{III}	$2p_{3/2}$	s, d
M_I	3s	p

Thus for a metal such as Cu, the K-edge XANES will probe 1s → 4p transitions and will provide information about the chemical environment of the Cu atom via the occupation of the 4p orbitals. Traditionally the term XANES is used when discussing the Near-Edge region of an XAS spectrum for a metal. The analogous study of this region of an XAS spectrum for "organic" or lighter elements is called Near-Edge X-ray Absorption Fine Structure (NEXAFS).

1.4 X-ray Photoelectron Spectroscopy

X-ray photoelectron spectroscopy (XPS) uses the principles of the photoelectric effect to study the electronic properties of materials. In a normal experiment, a beam of X-rays is directed at a sample inside a vacuum chamber. The incident X-rays can then be absorbed by a core level electron of the sample. These photoelectrons are subsequently ejected into the vacuum and travel towards the detector.

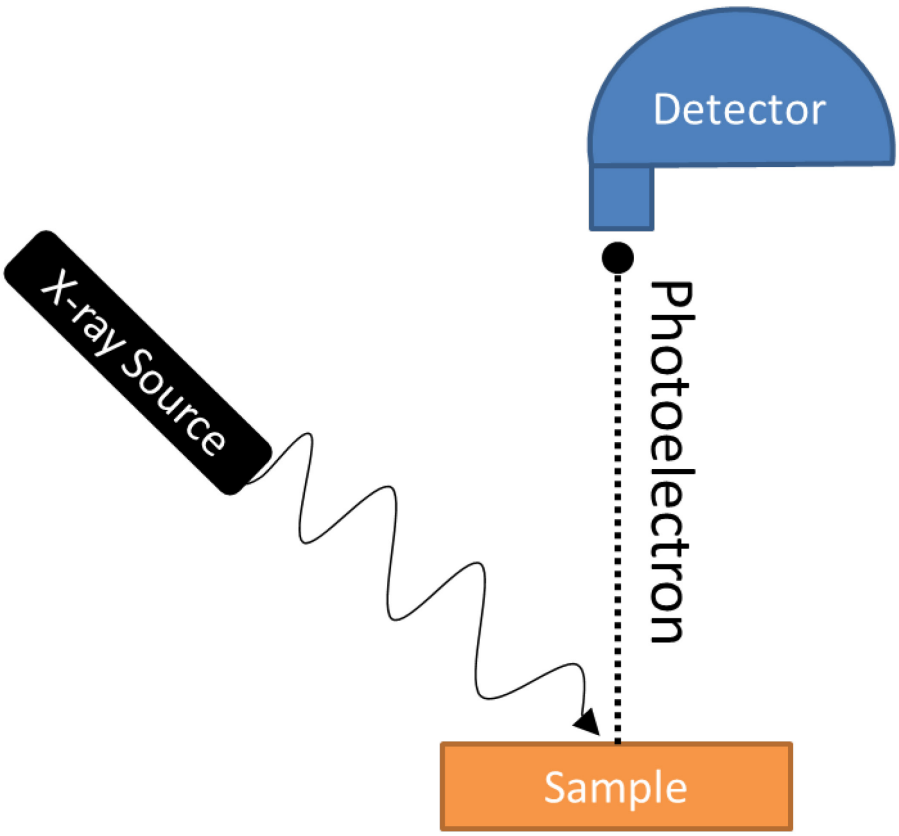

Figure 1-9: Illustration of the mechanism of photoelectron generation and detection in X-ray photoelectron spectroscopy. An incident X-ray is absorbed by a core level electron of the sample and ejected into the vacuum as a photoelectron.

The initial binding energy of the electron in the sample can then be determined by the relationship:

$$BE = hv - KE \tag{7}$$

where *BE* is binding energy of the electron, *KE* the measured kinetic energy of the photoelectron and *hv* is the energy of the incident photon. From the binding energy information about the chemical environment, atomic composition and electronic properties of the atom of study can be gained. This is achieved by monitoring and comparing the positions and profile of core level spectral features.

In practice the theoretical relationship (7) should be presented as:

$$BE = h\nu - KE + \phi \tag{8}$$

where ϕ represents the work function of the detector arising from the surface potential. This should be a constant value and can be calibrated for the instrument using a well-documented standard such as a gold foil.

1.5 *Ab Initio* Calculations

The use of *ab Initio* calculations to interpret XAS spectra has grown tremendously over past years.[32,35,36] Towards this end, the FEFF program code[32] is designed for the purpose of providing efficient calculations of XAS spectra to support and understand experimental findings.

In general, FEFF builds the molecular potential for a system of atoms surrounding (i.e. within a certain radius of) a designated absorbing atom based upon relativistic atomic potentials (Dirac-Fock) and the Cartesian coordinates of the system.[34,37] A series of approximations is made to reduce the computational cost, including replacing the electron wave function with the electron Green's function and the use of spherically symmetric muffin-tin potentials rather than full potentials. In addition, a self-consistent field loop is utilized to improve the quality of the calculated electronic structure. From this molecular potential, simulations of EXAFS, XANES and local density of states (l-DOS) can be produced.

For EXAFS simulations, FEFF calculates the effective scattering amplitude, phase shift and energy-dependent mean free path of the photoelectron wave emitted from

the absorbing atom.[38,39] This produces files for refinement of experimental EXAFS spectra, as well as simulation of $\chi(k)$ for qualitative comparison.

The local density of states calculated by FEFF provides atomic orbital occupation numbers, charge transfer and the DOS for a particular atom.[34,37] While lower in resolution when compared with modern calculations of band structure, the FEFF l-DOS is a useful tool for the interpretation of XAS spectra.

To simulate XANES spectra, FEFF calculates electronic transitions and multiple scattering excitations which occur in the low energy region (i.e. up to ~40 eV past E_o) of an XAS spectrum. This is done by considering the number and intensity of the multiple scattering paths possible around the absorbing atom.[32,34,37,39] Due to the large number of possible multiple scattering paths this calculation is typically performed for a cluster of defined size about the absorbing atom (~30 atoms).

1.6 Motivation

The goal of this work is to utilize a range of compositionally precise gold nanoclusters to provide a deeper understanding of the structure and electronic properties about specific atomic sites within the clusters via X-ray spectroscopy. This will aid in developing an understanding of the chemical and physical properties of these and other related nanomaterials.

CHAPTER 2: STRUCTURE AND BONDING OF Au_{144} NANOCLUSTERS

2.1 Introduction

Research into gold-thiolate nanoclusters (NCs) of precise composition has emerged as a rapidly growing area in nanoscience.[9,19,25,40] A variety of such NCs have recently been synthesized and studies on their structures and properties have attracted a great deal of interest.[41-44] At this size range (Au core size < 2nm) the electronic structure of these materials begins to deviate from that of larger nanoparticles, exhibiting new site-specific and size-dependent properties such as chemical stability[45,46] and catalytic activity.[47,48] As a result, fundamental questions have been raised about the origin of these new properties, and how they are correlated with specific atomic sites and overall size of the NPs.

The precisely controlled composition of these $Au_m(SR)_n$ NCs provides a great opportunity to explicitly illustrate the structure and bonding properties of these nanoclusters from a site-specific perspective. Understanding the bonding of specific atomic sites (e.g. surface, core and ligand sites), and how these change with NC size is critically important in developing mechanisms to explain the structure-property relationships of these NCs. Atomic structure determinations of $Au_m(SR)_n$ NCs by X-ray crystallography have been limited due to the inherent difficulties in sample crystallization,[20,21,49] thus, producing quantitative structural models of these materials

using alternative characterization tools is urgently needed.

Towards this end an X-ray absorption (gold L_{III}-, sulfur K- and L-edge) and photoemission (gold 4f, sulfur 2p and valence band) study of compositionally precise gold-thiolate nanoclusters is presented. First, an X-ray spectroscopy approach to illustrate the structure and bonding of $Au_{144}(SR)_{60}$ is demonstrated. In conjunction with *ab initio* calculations, a high-precision, atomic-site-specific illustration of the bonding in $Au_{144}(SR)_{60}$ is achieved. Finally, by comparing size-varied samples [$Au_{144}(SR)_{60}$, $Au_{38}(SR)_{24}$ and $Au_{25}(SR)_{18}$], size-dependent trends in the bonding of gold-thiolate NCs are revealed from both the sulfur and gold perspective via XAS.

2.2 Experimental

The syntheses of compositionally precise $Au_{144}(SR)_{60,}$ $Au_{25}(SR)_{18}$ and $Au_{38}(SR)_{24}$ (where R = PhC_2H_4S-) nanoparticles was conducted by Prof. R. Jin's group at Carnegie Melon University. Details of the synthesis have been published elsewhere.[20,22,29] The XAS experiments were conducted at the CLS (S K-edge at SXRMB beamline, S L-edge at PGM beamline and Au L-edge at HXMA beamline) and APS (Au L-edge at PNC/XSD beamline). XPS was collected both using a laboratory-based Multilab system by VG Thermo Scientific and at the SGM beamline of the CLS. The simulation of XAS and calculations of the angular momentum projected density of states (l-DOS) were conducted using the FEFF8 program.[34] Nanostructure models were obtained either from ref. 21 or provided by the corresponding author of ref. 50.

Refinement of the Au L_{III}-edge EXAFS was conducted using previously reported procedures.[51] Theoretical fitting standards were made using FEFF 8[34] and the previously reported crystal structure of Au_{102}.[25] A k-range of 3-11.7 $Å^{-1}$ and an R-range of 1.5-3.3 Å

were used during the refinement. One Au-S and one Au-Au path were used and error estimates were based upon the magnitude of the residual of the refinement.[52]

Deconvolution of Au-thiolate nanocluster S K-edge spectra was performed using three functions: 2 pseudo-Voigt line shapes fixed at a 50-50 Gaussian-Lorentzian mixing, and one arctangent function to serve as the background. Peak positions were constrained (i.e. ± 0.25eV) based upon local minima in the smoothed second derivative of the absorption spectra as per previously reported procedures.[53]

For further experimental details please see Appendix A.

2.3 Structure of Au_{144}

Au_{144} represents the largest nanocluster (~1.6 nm core diameter) to be synthesized in high yield and purity. Recent DFT calculations by Lopez-Acevedo et al. suggest that the packing structure of Au_{144} consists of a 114 atom core surrounded by 30 S-Au-S monomeric staple units.[50] The core is composed of three high symmetry Au-Au-shells with the smallest being a 12-atom icosahedron and the largest being a 60-atom rhombicosi-dodecahedron (Figure 2-1).

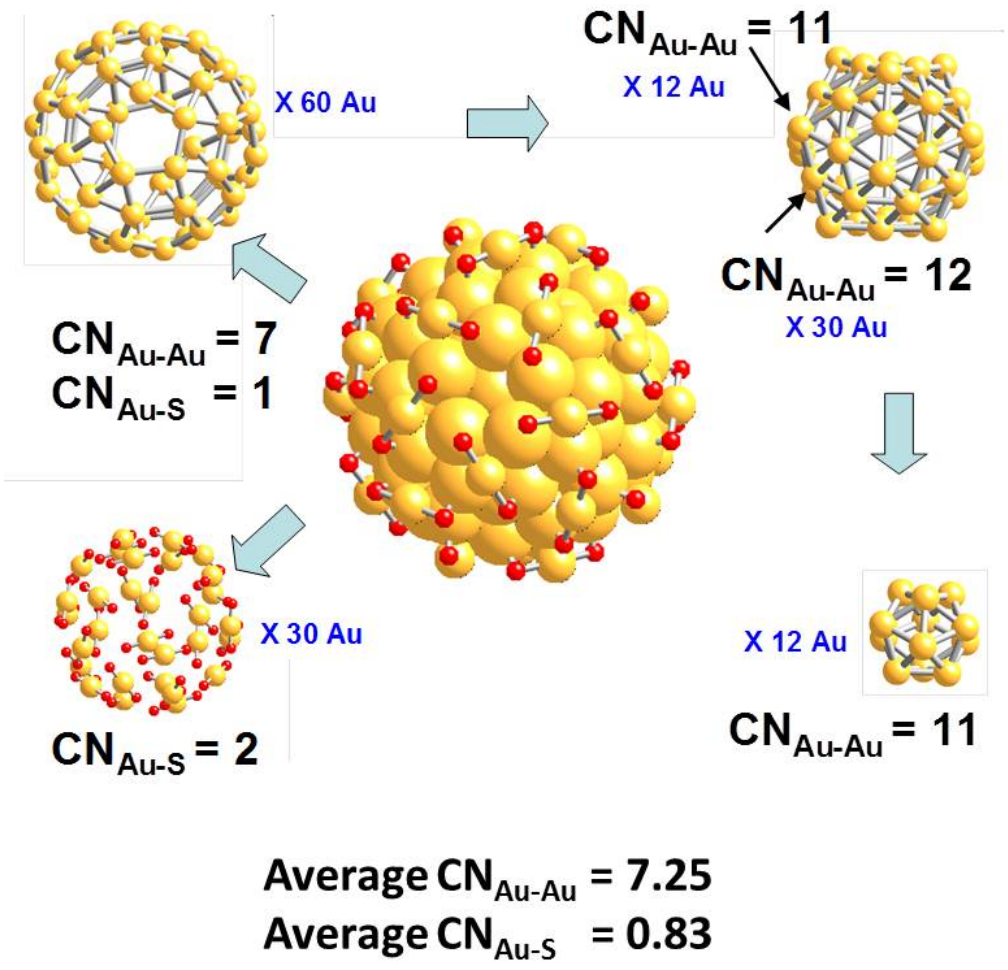

Figure 2-1: Proposed structure of $Au_{144}(SR)_{60}$ and the associated coordination environments of each sub-shell. The yellow atoms represent gold while red represents sulfur. The carbon tail attached to the sulfur has been omitted for clarity.

Due to the size of Au_{144}, the structure and bonding of this system is of particular interest for its possible extension to larger nanoparticle systems and self-assembled monolayers.

2.4 Results

2.4.1 EXAFS of Au_{144}

The XAS results for Au_{144} are shown in Figure 2-2. The X-ray absorption Near-Edge structure (XANES) (Figure 2-2, part a) shows an increase in white line intensity relative to that of bulk Au foil, signifying an increase in d-hole population in the valence band.[54] The *k*-space EXAFS of the nanoparticle shows a reduction in intensity of *k*-space oscillations relative to bulk Au, characteristic of nanoscale Au nanoparticles. A refinement of the FT-EXAFS was performed (*R*: 1.5-3.3 Å, *k*: 3.0-11.7 $Å^{-1}$) using theoretical scattering paths based upon the previously determined structure of Au_{102}.[25] Examining the fit results (Table 2-1) experimental evidence supporting the structure calculated by Lopez-Acevedo et al. is observed (Figure 2-1, Figure 2-2 part c). The resulting EXAFS experimental values show average coordination numbers (*CN*) of Au-S and Au-Au identical (within the uncertainty level) with those of the theoretical model (Table 2-1). Particularly the *CN* of the first-shell Au-S bond perfectly matches that calculated from the theoretical model. The *CN* of the first-shell Au-Au bond shows a higher uncertainty than that of Au-S bond, similar to the EXAFS results for smaller thiolate-Au nanoparticles recently reported.[51] This is accompanied by a high mean squared displacement (σ^2) of the Au-Au bond, most likely attributable to static disorder within the nanocluster and the aurophilic bonding between the surface Au and Au in the

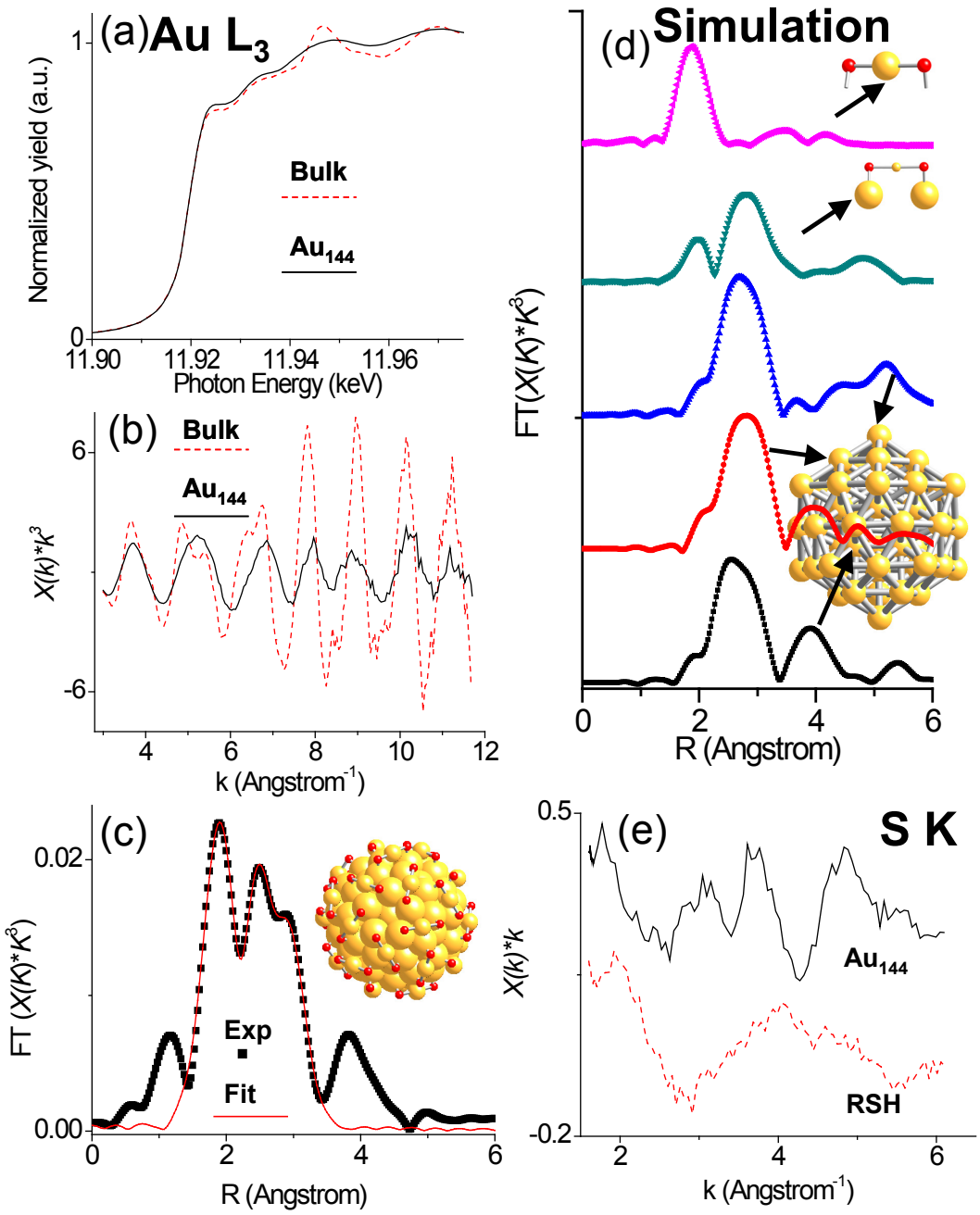

Figure 2-2: Au L_{III}- edge (a) XANES, (b) *k*-space EXAFS, (c) fitted FT-EXAFS , (d) simulated FT-EXAFS for staple (pink), surface (green) and core (blue, red, black) Au atomic sites and (e) S K-edge *k*-space EXAFS of Au_{144} and a free thiol reference (RSH). The Au L-edge measurement was conducted in air whereas S K-edge XAS was measured in vacuum. A gold foil was used as the bulk reference. The interatomic bond distances of the Au_{144} theoretical model were adjusted by applying a lattice contraction of 2.5% prior to the XAS simulation.

staples.[21] The precisely controlled composition of this nanoparticle allows for comparison of the experimental data with site-specific simulated EXAFS (Figure 2-2, part d) in order to verify the above fitting results, as well as to illustrate the origin of the experimental FT-EXAFS features. Comparing Figure 2-2 (c) and (d) it can be seen that the simulated EXAFS correlates well with the experimental spectrum. The peak at ~2Å (Figure 2-2, part c) is mainly originated from the Au-S bond in the staple with a smaller contribution from the Au-S bond between the surface Au and S. The peak next to the Au-S peak in the higher *R* region is related to the first-shell Au-Au bond of the nanocluster surface and core. Moreover, the FT-EXAFS peak at around 4 Å is largely associated with the second-shell (i.e. next nearest neighbor) Au-Au bond of the core Au atoms. Additionally, the sulfur (S) K-edge EXAFS of $Au_{144}(SR)_{60}$ together with that of a thiol reference (R-SH) (Figure 2-2, part e) is presented. Due to the presence of Au M_{III}-edge absorption above the S K-edge, the *k*-space spectrum can only be used up to ~6 $Å^{-1}$. Qualitative analysis of the spectra shows that the two S atoms are in distinctly different environments. Particularly there is an increased oscillation frequency in the EXAFS for the nanocluster sulfur versus the free thiol molecule. Thus, for the nanoparticle S the EXAFS is dominated by the presence of the longer S- Au bonds, while for RSH the EXAFS is mainly associated with the short S-C bond.

Table 2-1: Au L_{III}-edge EXAFS fitting results of $Au_{144}(SR)_{60}$. Theoretical coordination numbers were based upon the model proposed by Lopez-Acevedo et al.[50]

Bond	*R* (Å)	*CN*	*CN* (theoretical)	σ^2 ($Å^2$)	E_0 (eV)
Au-S	2.340(3)	0.83(6)	0.83	0.0052(6)	0.9(7)
Au-Au	2.831(2)	7.0(4)	7.3	0.0138(4)	-0.6(4)

2.4.2 Photoelectron Spectroscopy and l-DOS of Au_{144}

The core-level and valence band XPS of Au_{144} is shown in Figure 2-3. The Au 4f core level shows a ~0.20 ± 0.05 eV positive shift and a peak broadening of ~0.15 eV relative to Au foil, similar to that recently reported for $Au_{144\text{-}146}(SR)_{50\text{-}60}$.[17] Based on the atomic structure of Au_{144} determined above it is reasonable to fit the Au 4f spectra from a site specific perspective using three sets of doublets representing core, surface and "staple" Au environments in the appropriate ratios of Au_{core}: $Au_{surface}$: Au_{staple} = 54 : 60: 30, (Figure 2-3, part b). A systematic increase in the binding energies of these environments is also observed (i.e. 84.16 eV for core Au, 84.43 eV for surface Au and 84.85 eV for "staple" Au). These site-specific fitting results help to clearly illustrate the bonding behavior of the Au-thiolate nanoparticles. Specifically, the core Au atoms are of metallic nature (84.16 eV is characteristic of metallic Au);[55] the staple Au atoms are non-metallic (84.85 eV is typical for non-metallic Au)[55] and the surface Au atoms have mixed metallic and non-metallic bonding. An atomic ratio of 1:1.7 for Au_{staple} to S was obtained from the data, which is in good agreement with the theoretical Au_{staple} to S value of 1:2 considering the uncertainty of XPS composition analysis, and chemical transferability of atomic sensitivity factors. These results are in excellent agreement with the recently proposed superatom model,[56] which is used to account for the selective stability of certain of Au-thiolate nanoclusters.

The valence band XPS of Au_{144} (Figure 2-3, part c) shows a narrowing relative to that of the bulk Au by about 0.2 ± 0.1 eV. This is accompanied with a small reduction of the apparent spin-orbit splitting by 0.1 eV, which is considerably smaller than previous results for non-monodispersed nanoparticles of identical size.[54] The above valence band

results indicate that a compositionally precise $Au_{144}(SR)_{60}$ nanocluster, albeit of its small size of ~1.6 nm in diameter,[17] exhibits essentially an overall metallic behavior in terms of the valence band shape, consistent with observations by Taylor et al. for bare gas phase gold clusters.[57] The Au 5d-DOS behavior of the nanoparticles can be illustrated by performing calculation of the d-DOS for each specific site of Au_{144} shown in Figure 2-3, part d. The d-DOS of Au in the "staple" is the narrowest and a singlet in shape, indicative of its molecular behavior or non-metallic bonding nature. In comparison, the core Au site shows significantly wider d-DOS of a doublet shape, indicating its metallic behavior. The d-DOS shape of the surface Au site is somewhat between those of the other two sites, indicating that the surface Au should have mixed metallic and covalent bonding behavior.[56] In addition, a comparison of the weight-average d-DOS of all sites in $Au_{144}(SR)_{60}$ with that of bulk gold (theoretical) (Figure 2-3, part d) finds them in good agreement with the experimental results (Figure 2-3, part c). Inspection of the S 2p X-ray photoelectron spectrum (Figure 2-3, part e) shows a shift of binding energy (BE = 162.5 eV) to a slightly higher value than that of thiol in 2D and 3D SAMs[55] and can be fit with two peaks split by 1.2 eV with an appropriate ratio of $2p_{3/2}$:$2p_{1/2}$ = 2:1.[55]

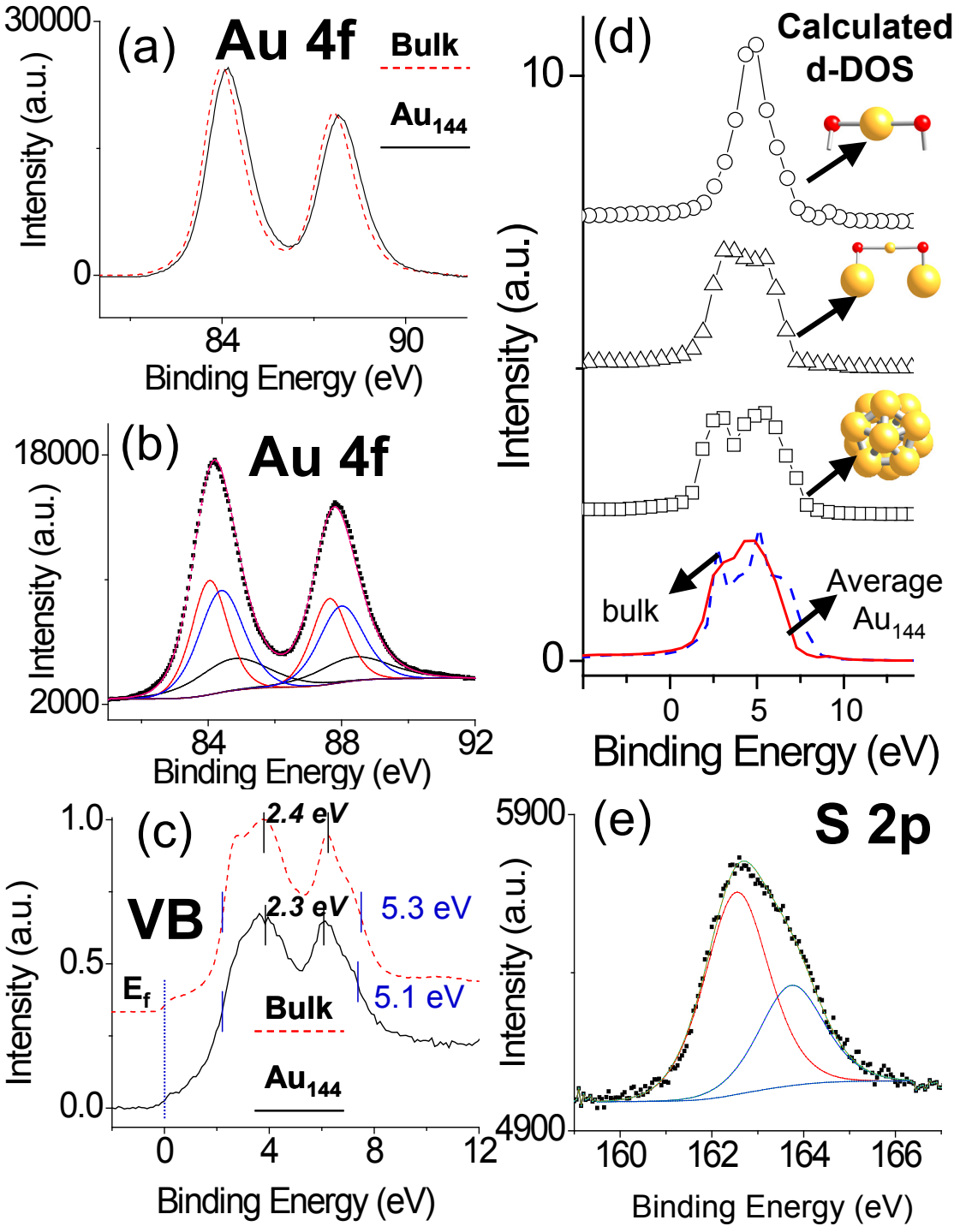

Figure 2-3: XPS spectra of (a) Au 4f core level, (b) Au 4f core level with fitting, (c) valence band region, (d) Simulated d-DOS and (e) fitted S 2p core level of Au_{144}.

2.4.3 NEXAFS of Au_{144}

The use of near-edge X-ray absorption fine structure (NEXAFS) at the sulfur K-edge is advantageous for studying the bonding of thiolate-based nanostructures, as sulfur has often been regarded as a spectroscopically silent element.[58,59] By performing *ab initio* calculations (NEXAFS and l-DOS) and using the atomic structure of Au_{144} the bonding of Au_{144} can be further illustrated from the sulfur perspective. Comparing both the simulated and experimental spectra near the S K-edge (Figure 2-4, part a) and $L_{III,II}$-edge (Figure 2-4, part b) indicates that the simulations produce essentially the same main features (**A**-**D**) of the spectra, thus proving reliable. The two main features (**C** and **D**) in the higher energy region are due to the EXAFS. The other two features (**A** and **B**) can be ascribed to S-Au and S-C resonances.[54,60] The S K-edge NEXAFS (Figure 2-4, part c) is selected for a closer inspection, as the S-Au feature near the K-edge is significantly more intense than near the $L_{III,II}$-edge. The s,p,d-DOS of the S, Au and C atoms in $Au_{144}(SR)_{60}$ are also displayed. The l-DOS of the Au and C atoms were calculated by selecting the S atom as the absorber, which ensures that only the l-DOS of the Au and C atoms bonding to the S atom are included in the calculation.[34] The simulated NEXAFS using a model nanoparticle without carbon atoms, referred to as $Au_{144}S_{60}$, is also shown. As is seen in Figure 2-4, part c, feature **a** and **a'** (corresponding to feature **A** in Figure 2-4, part a) are observable at essentially the same position for both $Au_{144}(SR)_{60}$ and $Au_{144}S_{60}$, indicating that these two features are originated from the S-Au bonding. Note that these two features are only seen as one pre-edge feature in the experimental data due to the limited instrumental resolution. In comparison, feature **b** (corresponding to feature **B** in Figure 2-4, part a) is absent in the simulated NEXAFS of $Au_{144}S_{60}$, evidence that this feature is

associated with the S-C resonance. As is seen in Figure 2-4, part c, feature **a** and **a'**, correspond to Au-S antibonding states,[54,60] and are related to unoccupied S 3p- and Au 5d/6s-states with small contributions possibly from the unoccupied S d- and Au p-states. Feature **b** can be assigned as a transition into S-C σ^* orbitals with contributions from the unoccupied S p/d-states and C p-state.

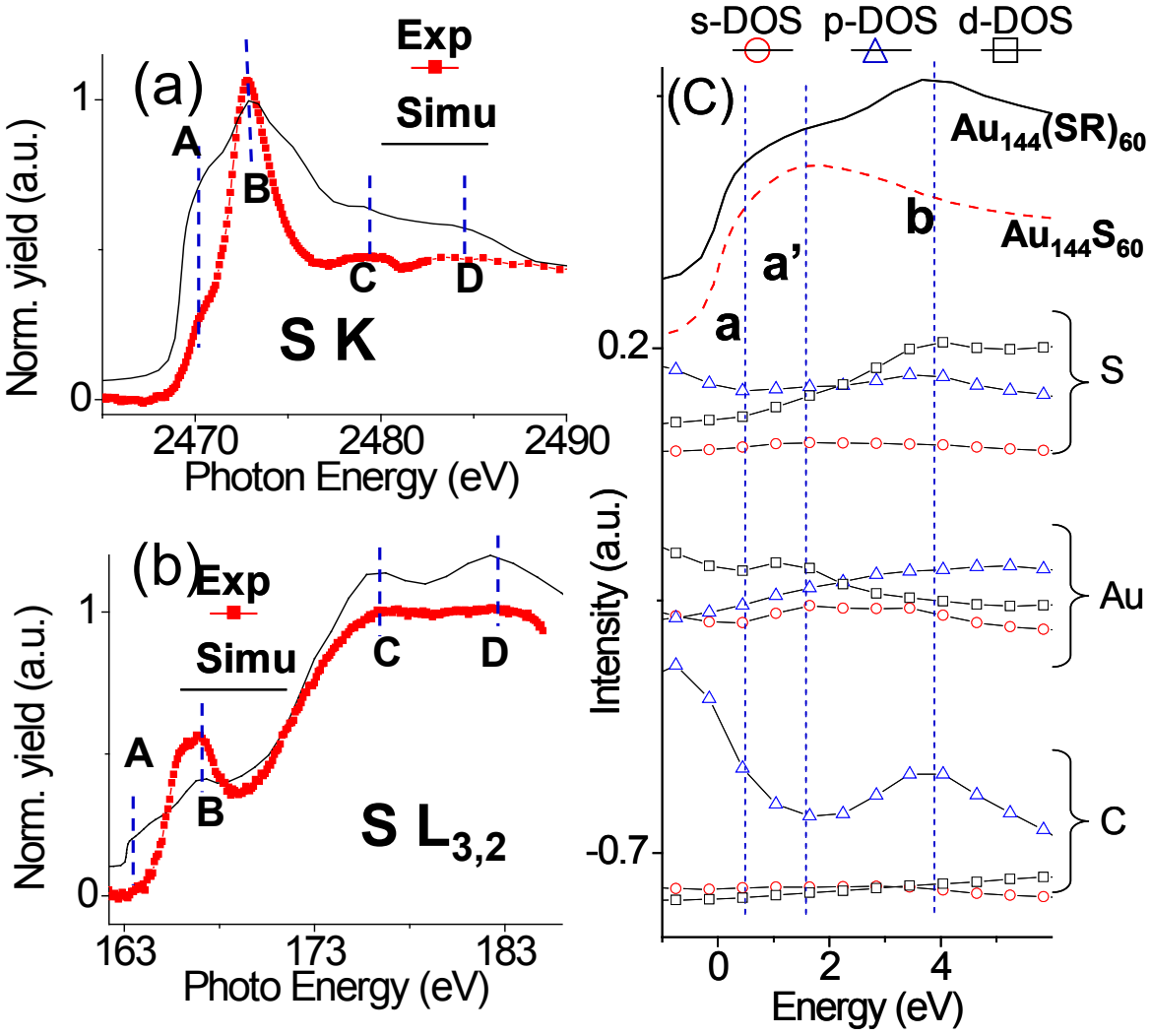

Figure 2-4: XAS of (a) S K-edge, (b) S $L_{III,II}$-edge and (c) S K-Edge XAS simulations with and without carbon and l-DOS results.

Thus by inspecting the S NEXAFS region of XAS spectra information about the bonding between sulfur and gold may be obtained by observing the shape and position of feature **A**.

2.4.4 Size dependent trends of gold nanoclusters

Finally, a comparison of the bonding of Au_{144} to smaller Au-thiolate nanoparticles is presented. In Figure 2-5 the experimental S K-edge NEXAFS of Au_{25}, Au_{38} and Au_{144} are displayed. For a discussion of the structures of Au_{38} and Au_{25} please see sections 3.3 and 4.3.

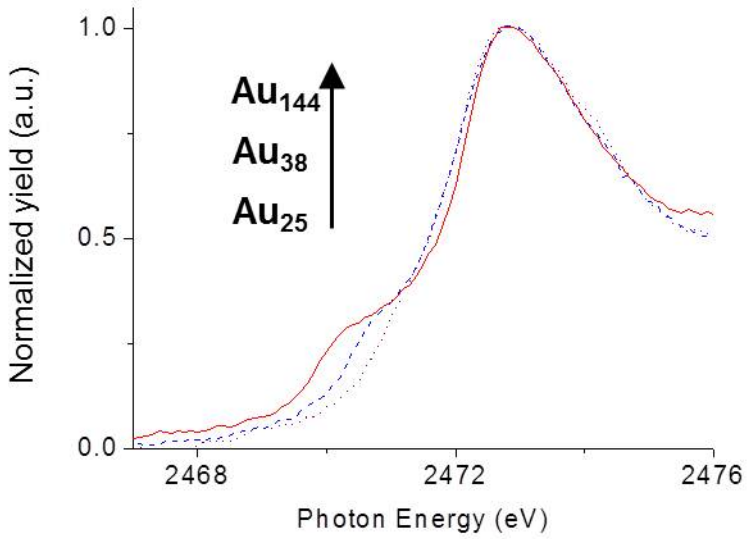

Figure 2-5: Sulfur K-edge NEXAFS of size-varied Au-thiolate nanoclusters. The pre-edge feature grows in intensity with cluster size.

The most interesting observation is the increase in intensity of the S-Au pre-edge feature with nanoparticle size. S K-edge NEXAFS allows for the examination of the covalent components (non-metallic Au bonded to S) of these Au-thiolate nanostructures, providing insight to the electronic properties of this environment independently from the metallic Au-core. By fitting these NEXAFS spectra (Figure 2-6) using the established procedure for metal-thiolate NEXAFS fitting,[53] the S-Au NEXAFS features in the three samples are found to show a red-shift (Table 2-2) in peak position as the size increases, that is, 2471.1 eV for Au_{25}, 2470.7 eV for Au_{38} and 2470.5 eV for Au_{144}. This is accompanied by an increase of the fitted S-Au relative peak intensity, which is 0.064 for Au_{25}, 0.122 for Au_{38} and 0.207 for Au_{144}. A consistent size-dependent increase of the S-Au peak intensity is also found when comparing the S K-edge NEXAFS spectra of Au_{144}, Au_{38} and Au_{25} with those for larger Au nanoparticles.[54,60]

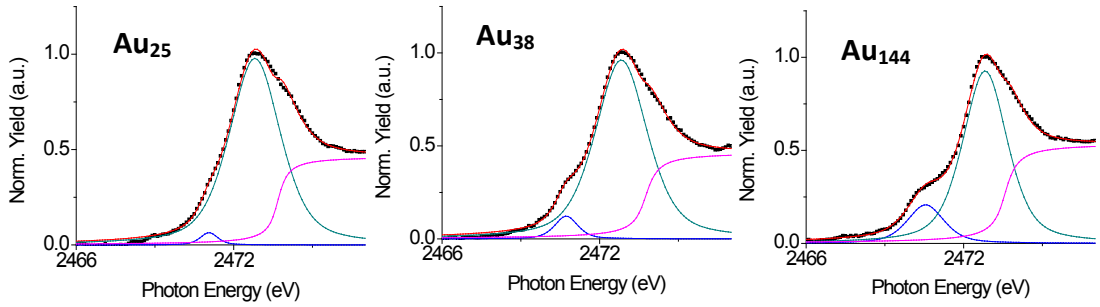

Figure 2-6: Deconvolution of Au-thiolate nanocluster S K-edge spectra. The clusters are identified by the number of gold atoms (25, 38, 144) marked above. Contributions from the S-Au (blue) and S-C (green) resonances were added, along with a background function (pink). The total fit (red) is overlaid on the experimental data (points) for comparison.

Table 2-2: Fit results of S K-edge XAS of gold-thiolate nanostructures. The intensity of the original spectra were scaled to make the S-C resonance ~1 a.u.

Compound	Feature	Position (eV)	Intensity	Area (eV)	FWHM (eV)
$Au_{25}(SR)_{18}$	Peak 1	2471.06	0.064	0.065	0.79
	Peak 2	2472.81	0.978	2.752	2.32
	Background	2473.69	0.465	1.583	0.89
$Au_{38}(SR)_{24}$	Peak 1	2470.73	0.122	0.161	1.03
	Peak 2	2472.83	0.962	2.747	2.36
	Background	2473.76	0.466	1.56	1.11
$Au_{144}(SR)_{60}$	Peak 1	2470.55	0.207	0.428	1.65
	Peak 2	2472.82	0.927	2.287	2.01
	Background	2473.58	0.539	1.899	1.12

In order to gain insight towards the origin of these results a comparison of the Au d-DOS, Au s-DOS and S p-DOS is made based on the experimentally determined structures of Au_{25}[21] and Au_{144} calculated using S as the absorbing atom (Figure 2-7). For simplicity, the analysis is limited to these two nanoclusters due to their structural simplicity (i.e. spherically symmetric and only one type of staple site) and significant size difference (~1 nm versus 1.6 nm). As is shown in Figure 2-4, the S-Au bonding feature in the NEXAFS is mainly distributed in the region of 0-2 eV above the Fermi level. Therefore, particular attention is placed on this region, which is marked by dashed lines (Figure 2-8). The most interesting observation is that the unoccupied Au s- and d-DOS in the region of 0-2 eV above the Fermi level both show a red-shift and an increase in intensity when going from Au_{25} to Au_{144}. Since the same size-dependent trend is also observed for the S-Au NEXAFS pre-edge feature (Table 2-2) it suggests that the size-dependent nature of the S-Au NEXAFS feature should be directly related to the evolution

of the unoccupied Au s- and d-DOS.[35,61] Furthermore, the unoccupied S p-DOS in the same region shows an opposite trend compared to that of the Au s- and d-DOS, thus as the nanostructure size varies the extent of hybridization between the unoccupied S p-states and Au s-/d- states changes correspondingly. Whereas the final states for the observed transitions in S-Au NEXAFS are of a highly mixed origin,[35] it seems the experimentally observed red-shift and intensity enhancement of the S-Au NEXAFS feature with nanostructure size should be largely contributed to the evolution of unoccupied Au s/d-DOS mixed with S p-DOS. A more detailed analysis of this electronic structure evolution by high resolution theoretical approaches (i.e. time dependent density functional theory) should shed deeper insight onto these observations. Particularly, knowing how this electronic structure evolution depends upon surface-staple bond distance and the local geometry around sulfur in the staple unit will prove useful in understanding the structure-property relationships of these materials.

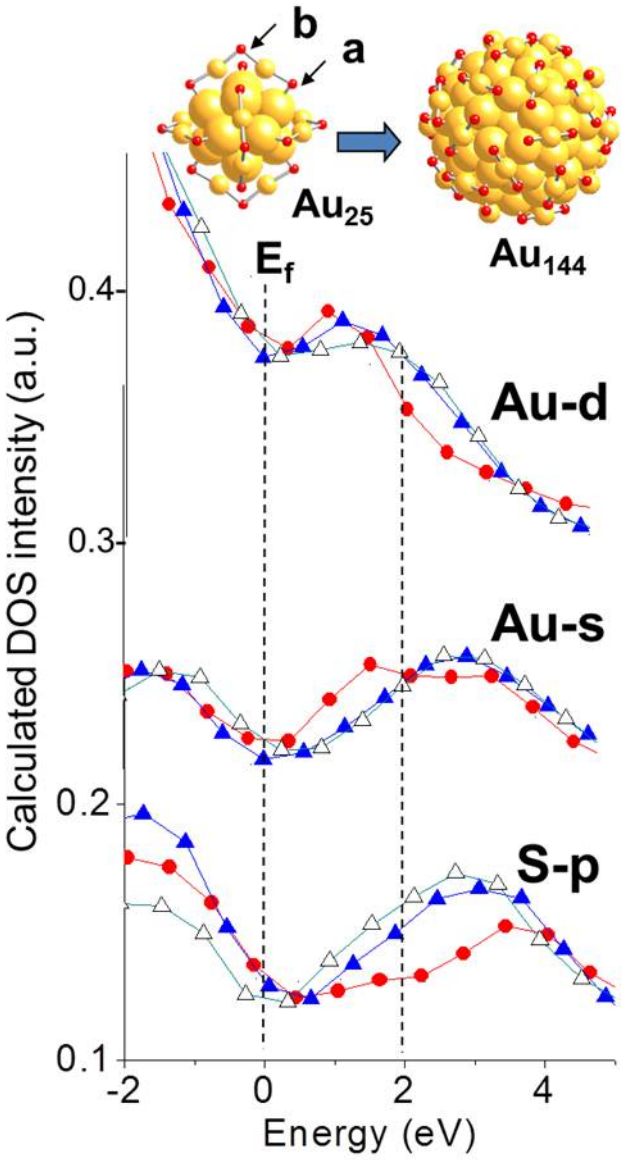

Figure 2-7: Simulated l-DOS of $Au_{25}$and Au_{144} with S as the absorbing atom. The S-p, Au-s and Au-d DOS for Au_{25} site a (▲), site b (△) and Au_{144} (●) are presented.

The Au L_{III}-edge XANES of the three nanoparticles and bulk Au is presented in Figure 2-8. The first feature of the Au L_{III}-edge XANES probes 2p to unoccupied 5d states for all the Au atoms in the nanoparticles,[56] therefore, results in Figure 2-8 are complementary to S K-edge NEXAFS in probing the bonding in these nanostructures.

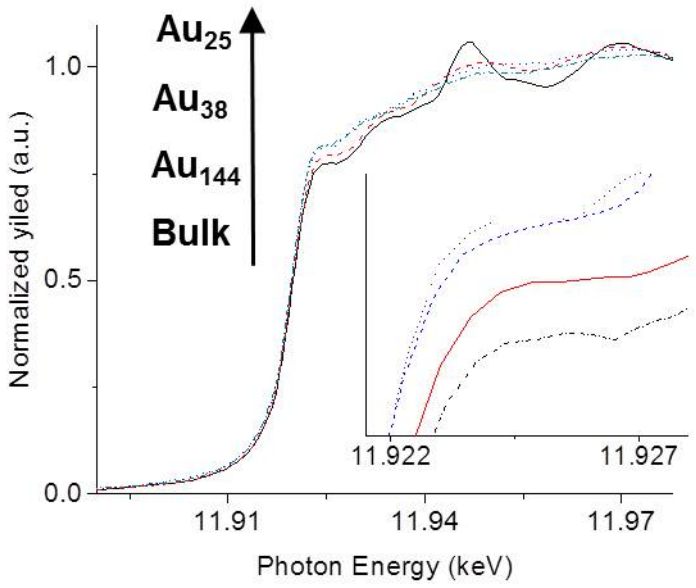

Figure 2-8: Au L_{III}-edge XANES spectra of size varied gold-thiolate nanocluster samples compared to gold foil. A general increase of white line intensity can be observed with size reduction.

As shown from the comparison of the XANES for all the clusters (Figure 2-8, inset), the Au L_{III}-edge white line intensity increases in the order of bulk Au → Au_{144}→ Au_{38} →Au_{25}, indicating a d-electron depletion as the size decreases.[54] Analyzing the theoretical d-hole counts using model nanoparticles of Au_{25} and Au_{144} it is observed that relative to the bulk Au, staple Au sites shows a more pronounced d-electron depletion than core Au sites. Therefore, the observation of the increased d-hole counts reflects the increased fraction of staple Au environments as the nanoparticles become smaller.

2.5 Conclusion

In conclusion, a site-specific and size-dependent study of the bonding in Au-thiolate NPs using truly monodisperse samples, the staple gold-thiolate bonding model and multi-element, multi-core X-ray techniques associated with *ab initio* calculations has

been presented. The atomic structure of $Au_{144}(SR)_{60}$ has been determined from EXAFS and a high-precision, atomic-site-specific illustration of its bonding has been presented. By extending the X-ray studies to smaller nanoparticles, the size-dependent nature of Au-thiolate and Au-Au bonding in these nanoparticles is systematically presented from a site-specific perspective.

CHAPTER 3: SOLVATION DEPENDENT BONDING IN Au_{38} NANOCLUSTERS

3.1 Introduction

Recently, intense research has been directed at the study of quantum-sized gold-thiolate nanoclusters.[9,10,19] Understanding the atomic structure and structure-property correlation of these clusters is critical for both fundamental studies[35,56,62-64] and technological applications of nanomaterials.[13,48,65] Whereas the synthesis and many potential applications of these clusters occur in solution, an understanding of their atomic structure and properties in a solvated environment is of significant importance and interest. Recent studies by Toikkanen et al. have shown that solvation effect(s) can substantially influence the surface reactivity of Au_{38} clusters[44], however, a precise determination of the solution-phase structure and variation of bonding of these clusters upon solvation has been lacking.

Towards this end an Au L_{III}-edge X-ray absorption spectroscopy (XAS) study, including extended X-ray absorption fine structure (EXAFS), X-ray absorption Near-Edge structure (XANES), and *ab initio* calculations of the electronic properties of the Au-thiolate cluster Au_{38} in solution and the solid phase is presented. A significant expansion of the Au-S and Au-Au bonds associated with an increase of Au d-electron density of states (DOS) for Au_{38} upon solvation has been observed. These findings are accounted for by *ab initio* calculations of projected DOS, which further illustrate the unique

electronic behavior of Au_{38} from a site-specific perspective. Finally, the impact of these findings on tuning the properties of Au-thiolate clusters is discussed.

3.2 Experimental Methods

The synthesis of Au_{38} nanoclusters was conducted by Prof. R. Jin's group at Carnegie Melon University. Details of the synthesis has been reported elsewhere.[29] The Au L_{III}-edge EXAFS measurements were conducted in transmission mode at the HXMA beamline of the CLS operated at 2.9 GeV. A Si (111) monochromator crystal was used in conjunction with rhodium mirrors. For solid-state measurements a toluene solution of Au_{38} was drop-cast onto Kapton® tape and folded until ample signal was observed. Solution-phase measurements were recorded by dispersing Au_{38} in toluene in a teflon sample cell. The stability of samples in toluene was examined by UV-Vis, which showed that the clusters remain unchanged before and after EXAFS measurements.

Data processing was performed using the WinXAS program[66] and standard procedures[51,52] and error analysis.[52] Simulation of EXAFS phase and amplitude and calculation of angular momentum density of states (l-DOS) was performed using the FEFF 8[34] program code and the crystalline structure of Au_{38} recently reported.[67] Only one carbon atom/per sulfur was included in the model to save computing time.

The fitting procedure was performed on the k^3-weighted FT-EXAFS from 3-12.3 $Å^{-1}$. Refinement was performed via a nonlinear least-squares method in *R*-space with a window of *R*: 1.5-3.2 Å. Theoretical values of Au-S and Au-Au coordination number were determined from the total structure of Au_{38}. One group of Au-S bonds was determined to have a total coordination of 1.26, while two groups of Au-Au bonds can be identified in the Au_{38} cluster. The first group is the shorter Au-Au bonds with a total *CN*

of 3.3 whereas the second group is longer ones with a total *CN* of 3.5. The damping factor, S_0^2, was fixed at 0.9 (deduced from the fitting of Au foil) while all E_0 values were correlated. All other parameters (R and σ^2) were allowed to run free.

For further experimental details please see Appendix A.

3.3 Structure of Au_{38}

The Au_{38} nanocluster consists of a face fused biicosahedral core surrounded by three monomeric and six dimeric staple units (Figure 3-1). The monomeric staples are distributed around the shared face of the biicosahedron while the dimeric staples are distributed around each end of the nanocluster. The structure is closely related to the Au_{25} nanocluster and can be thought of as a face-sharing dimeric version of Au_{25}.

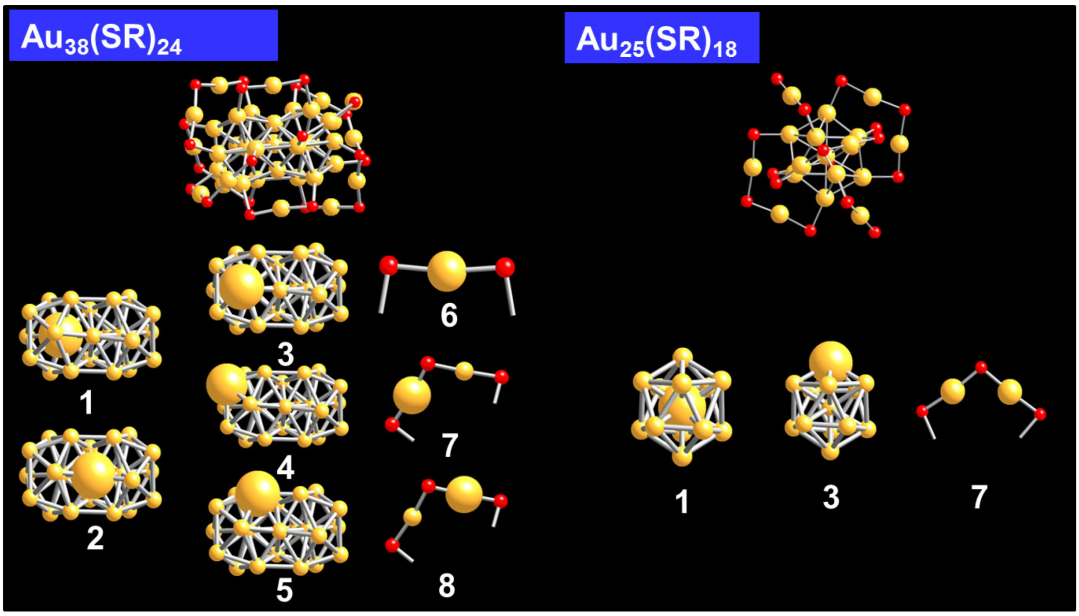

Figure 3-1: An illustration of the representative atomic sites of Au_{38} and Au_{25} used for l-DOS calculations. The red spheres represent sulfur, ligands while yellow represents gold. All other atoms (carbon, hydrogen) have been omitted for clarity.

There is a high degree of structural disorder in the structure of Au_{38}. This makes break-down of the structure for EXAFS refinement difficult. In this regard two Au-Au paths will be used during EXAFS refinement to observe the relative difference in bonding environment of the cluster in the solid state and in toluene.

3.4 Results

3.4.1 EXAFS analysis of Au_{38}

Figure 3-2 shows the experimental *k*-space and Fourier transformed (FT) EXAFS data along with expansions highlighting the difference of Au-S and Au-Au bonding between the solid and solution-phase Au_{38} clusters. The oscillation frequency of EXAFS has been known to be sensitive to the bond lengths surrounding the absorbing atom(s) in a material.[68] Qualitative comparison of the EXAFS (Figure 3-2, part a) of the solution-phase (in toluene) and solid samples clearly reveals an increase in overall oscillation frequency and decrease in intensity upon cluster solvation, corresponding to a general increase in bond length(s). This effect can also be observed in the FT-EXAFS showing a shift of the first-shell Au-S and Au-Au features to a higher value of *R* (Figure 3-2, part b).

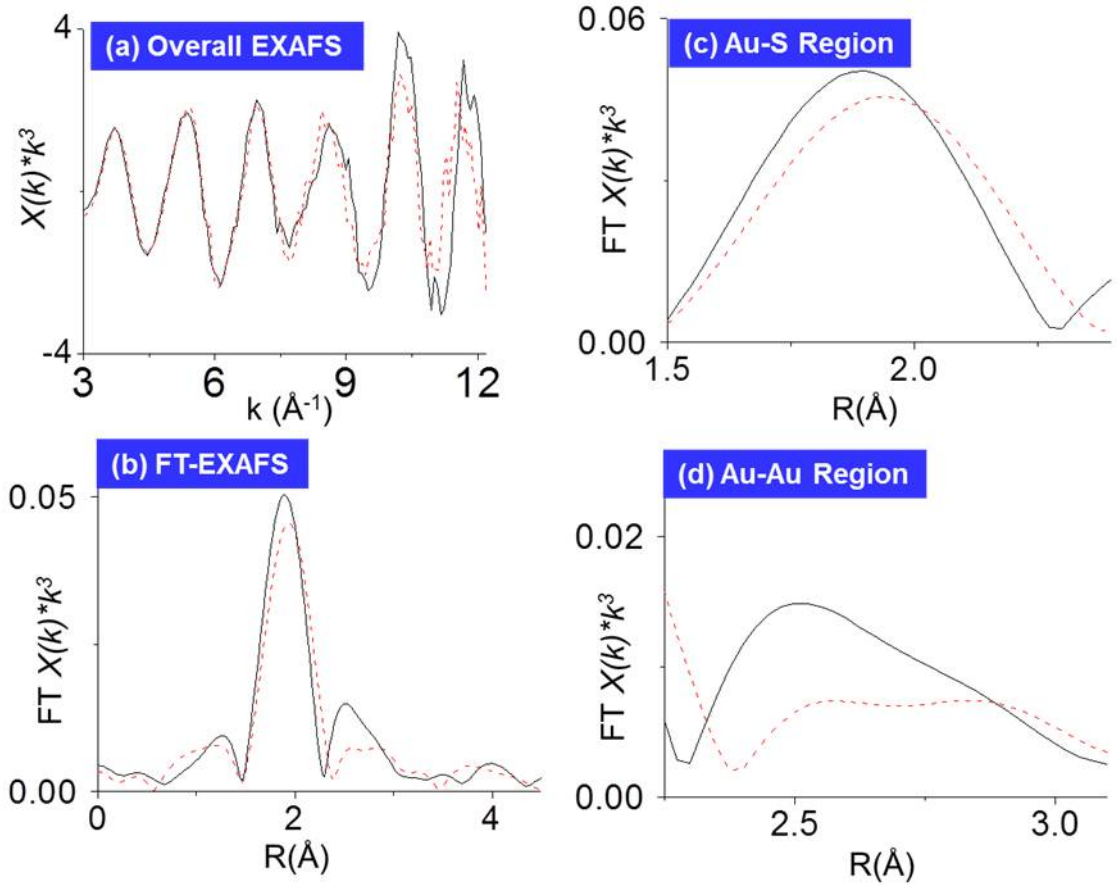

Figure 3-2: Solid state (—) and solvated (---) (a) $\chi(k)*k^3$ (b) FT[$\chi(k)*k^3$] and zoom-ins of the Au-S (c) and Au-Au (d) regions of the FT[$\chi(k)*k^3$] spectra for Au_{38}. The solvation-induced expansion of Au-S and Au-Au bonds can be qualitatively observed by the shift of the FT-EXAFS features to higher values in R-space. The more significant shift in the high k-region (a) implies a larger solvation induced shift for Au-Au bonding (d) than Au-S (c).

In order to obtain quantitative structural information, refinement of the FT-EXAFS was performed based on the recently determined total structure of the Au_{38} cluster[67] using one shell of Au-S and two shells of Au-Au (Figure 3-3 and Table 3-1). In comparison to the solid sample a general bond lengthening of 0.02-0.07 Å upon cluster solvation (Table 3-1) has been observed.

Table 3-1: EXAFS fitting data of solution-phase and solid-state Au_{38}. The *CN*s obtained from the total structural data were fixed and E_0 was correlated to be equal. All other variables were extracted from the refinement.

Sample	Path	*CN*	*R* (Å)	*ΔR* (Å)	σ^2(Å^2) x10^{-3}	E_0 (eV)
Au_{38} liquid	Au-S	1.26	2.346(3)	0.021	2.3(1)	3.7(6)
	Au-Au	3.3	2.820(7)	0.031	9.7(6)	3.7(6)
	Au-Au	3.5	3.032(10)	0.067	12.7(1)	3.7(6)
Au_{38} solid	Au-S	1.26	2.325(4)	-	1.5(2)	1.0(5)
	Au-Au	3.3	2.789(7)	-	7.4(8)	1.0(5)
	Au-Au	3.5	2.965(12)	-	10.8(14)	1.0(5)

The shorter Au-Au bonds (~2.8 Å) show lengthening to a much lesser extent than the longer bonds. Results on the total structure of Au_{38} indicate that the shorter Au-Au bonds are mainly associated with the interaction between the central Au atoms and the icosahedral surface Au atoms whereas the longer bonds come from the surface-surface and surface-staple Au interactions.[67] Therefore, it is understandable that the outer shell Au-Au bonds experience a more pronounced structural change caused by solvation than the center-surface Au bonds.

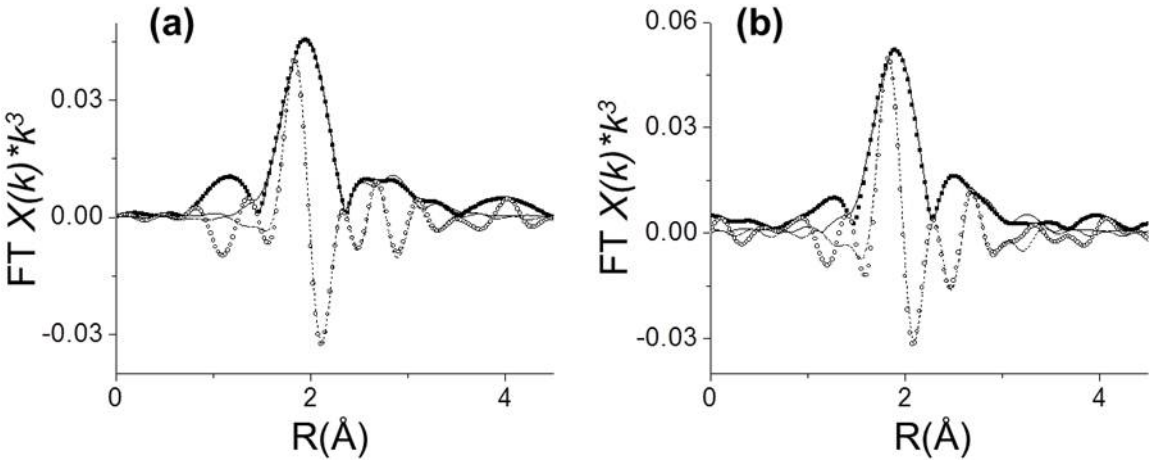

Figure 3-3: Absolute (■) and imaginary (○) components of the experimental FT[$\chi(k)*k^3$] for (a) solution phase and (b) solid state Au_{38}. Refinement of the absolute (—) and imaginary (---) spectra reveals a solvation induced bond expansion of approximately 1% when the clusters are dispersed in toluene.

The simulated EXAFS spectra in Figure 3-4 illustrate the site specific coordination environments of each atomic site within Au_{38}. The feature at 1.8 Å is attributed to Au-S bonding, and thus is only observable for surface and staple environments (Figure 3-4). All other features from 1.8-3.8 Å are a result of Au-Au single scattering paths. It can be seen that for sites with relatively high Au-Au coordination numbers (Figure 3-1, sites 1 and 2) the EXAFS spectrum resemble those of bulk gold, while surface sites have a mixture of short and long Au-Au interactions. Aurophilic interactions between staple sites and surface sites normally appear around 3.5 Å and are quite significant in this particular nanocluster. In general Au-Au coordination numbers are quite low for surface sites versus core sites, and thus aurophilic interactions could play a role in the observed solvation induced structural changes.

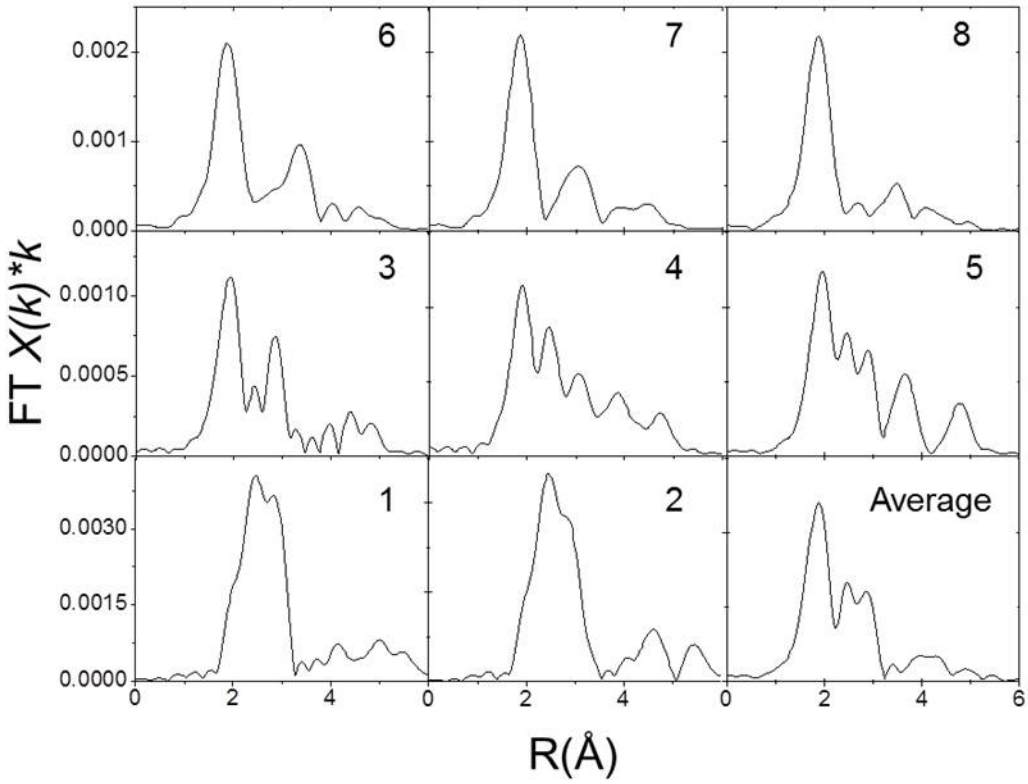

Figure 3-4: Simulated Au L_{III}-edge FT-EXAFS of each atomic site in Au_{38}. All sites are labeled as per Figure 3-1. All spectra were generated using then FEFF 8 program code and the recently reported total structure of Au_{38}. The feature at approximately 2 Å corresponds to Au-S bonds while all features at higher value of *R* correspond to Au-Au bonding.

A bond expansion of 0.02 Å upon solvation has been previously found in solution-phase EXAFS studies of a mercury (II) chloride compound, which was likely a result of the strong solvation of the Hg(II) cation by the solvent (dimethylsulfoixde).[69] In this case, it is unlikely that the solvent (toluene) directly interacts with gold atoms in Au_{38} to cause the bond expansion, however, it is plausible that through the aromatic interaction between the $–CH_2CH_2Ph$ moiety in the thiolate ligand and the solvent molecule (CH_3Ph) the Au-S and Au-Au bond distances are expanded in order to achieve a more favorable ligand-solvent interaction to stabilize the system. Nevertheless, a conclusive mechanism has to await further studies.

3.4.2 Au L_{III}-edge XANES results and l-DOS calculations

The near-edge region of an XAS experiment can be very useful in probing the electronic structure of gold nanomaterials.[51,64,68,70] In an L_{III}-edge experiment the XANES region is used to provide information regarding Au d-hole counts ($d_{hole} + d_{electron} = 10$). Electronic transition dipole selection rules allow L_{III}-edge XANES to selectively probe transitions between occupied 2p and unoccupied 5d states near the Fermi level. As a result higher d-hole counts (more unoccupied d-DOS near the Fermi level) corresponds to more intense X-ray absorption near the absorption threshold E_0. Upon comparison of the solvated and solid state Au_{38} XANES (Figure 3-5), a noticeable increase of Au 5d-electron density (i.e. decrease of d-hole counts or decrease of X-ray absorption intensity near E_0) for the solution-phase Au_{38} is observed.

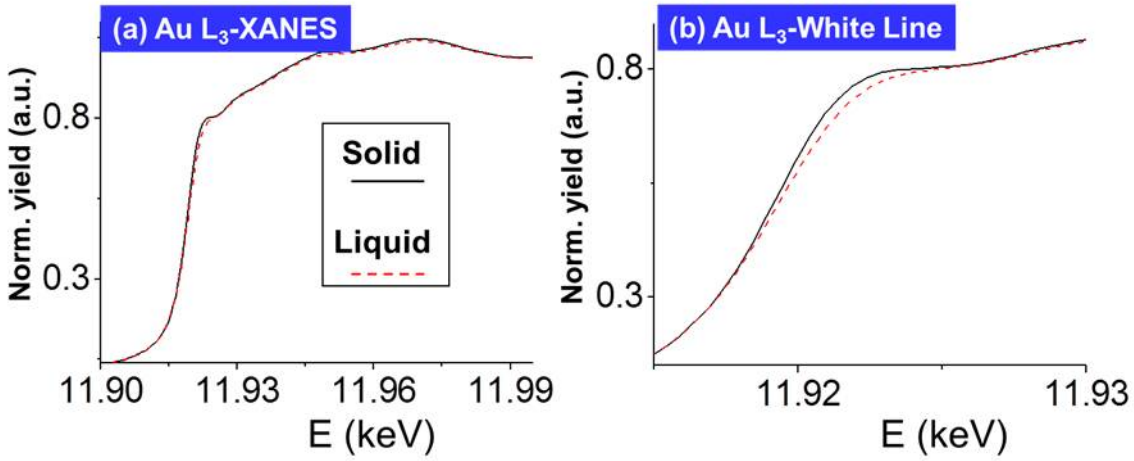

Figure 3-5: a) XANES spectra and (b) white line of solid state(—) and solvated (---) Au_{38}. The decrease in white line intensity upon cluster solvation in toluene corresponds in an increase of d-band occupation.

By conducting site- specific calculations of the Au d-DOS the same trend in d-electron counts for every atomic site across the cluster upon 1% bond expansion (Figure 3-6) is found. The observed increase of d-electron density upon solvation of Au_{38} can be accounted for by considering the d-charge transfer associated with Au-S bonding. For the solid sample, a shorter Au-S bond corresponds to more efficient d-charge transfer from Au to S than in longer bonds. As a result, the solvated sample containing longer Au-S bonds exhibits higher d-electron density (lower d-hole counts, Table 3-2).

Table 3-2: l-DOS calculation results of Au_{38} using FEFF 8.2. The labels represent charge transfer (q) and electron occupation of atomic orbitals (s, p ,d) about local atomic sites in Au_{38} with and without a 1% lattice expansion.

	Au_{38}				**Au_{38} with 1% Lattice Expansion**			
Site	q	s	p	d	q	s	p	d
1	0.268	0.779	0.677	9.275	0.248	0.785	0.668	9.3
2	0.142	0.844	0.661	9.353	0.127	0.851	0.648	9.374
3	0.202	0.848	0.663	9.287	0.208	0.848	0.643	9.301
4	0.135	0.856	0.727	9.282	0.131	0.859	0.709	9.301
5	0.144	0.844	0.714	9.299	0.132	0.85	0.699	9.319
6	0.202	0.939	0.686	9.175	0.220	0.933	0.664	9.183
7	0.182	0.938	0.69	9.191	0.175	0.941	0.673	9.212
8	0.194	0.929	0.69	9.186	0.187	0.932	0.673	9.207

To gain a deeper understanding of the electronic properties of Au_{38} *ab initio* l-DOS calculations were performed using the FEFF 8 code. The l-DOS calculations employ a self-consistent real Green's function that has been found to be in good agreement with modern calculations of band structure, even when relativistic effects are considerable.[34] Figure 3-6 shows the calculated d- and s-electron counts of the original and expanded Au_{38} model clusters. As a reference, the results for Au_{25} are also presented. A survey of the d- and s-electron counts indicates that staple Au atoms in both Au_{38}

and Au_{25} clusters (Figure 3-1, sites 6-8) show lower d- and higher s-electron counts than non-staple Au (Figure 3-1, site 1-5). It has been suggested that the Au-S interaction involves electron donation from the S lone-pair electrons to Au 6s states and a back-donation from Au 5d to S 3d states.[71] The calculation results in Figure 3-6, part a and b, clearly demonstrate the significance of this donation/back-donation bonding mechanism in the staple motif by showing the Au 5d count decrease (donation) and 6s count increase (back-donation). In comparison, such a bonding feature is not evident from the d- and s-electron counts of non-staple Au sites, most likely due to the perturbation of metal-metal bonding among these Au atoms.

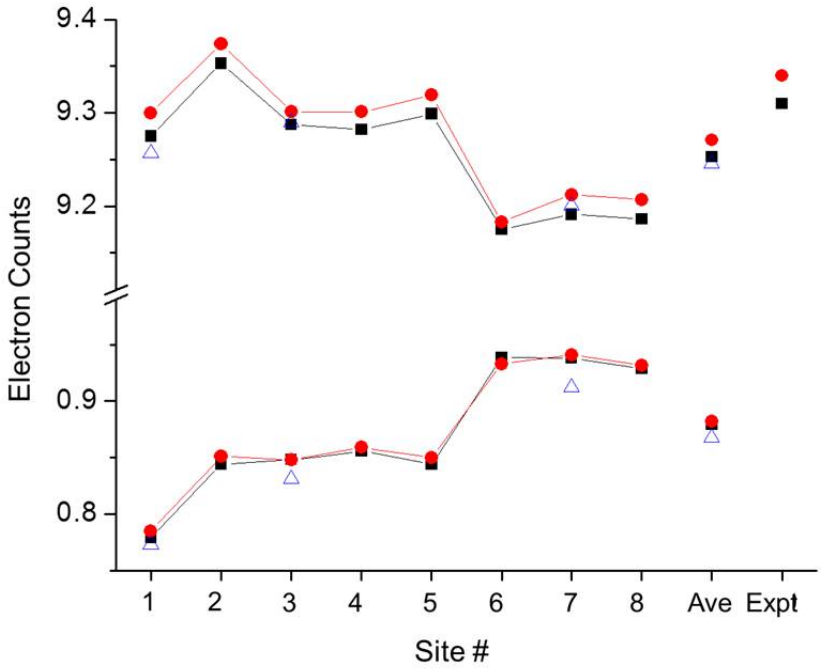

Figure 3-6: Calculated 5d and 6s electron counts distribution across each atomic site of Au_{38} (■), lattice expanded Au_{38} (●), and Au_{25} (Δ). A 1% lattice expansion was used to simulate the effect of solvation upon the structure of Au_{38}, while Au_{25} shows the effect of cluster size upon the electronic properties of similar atomic sites.

A close inspection of the d-DOS of Au_{38} and Au_{25} indicates that the former shows slightly higher average d-electron counts than the latter (Figure 3-6, part a). Notably, the Au site (Figure 3-1, site 2) in the fusion plane of the biicosahedral Au_{23} core shows substantially higher d-electron density than all other sites of the two clusters, which can be understood by the lower Au-Au coordination numbers and absence of direct Au-S interactions, signifying the unique d-electron behavior of Au_{38} associated with this site (absent in Au_{25}).

Moreover, Au_{38} possesses higher s-electron counts at each atomic site than Au_{25} and shows a general trend of increased s-electron counts upon bond expansion. The only exception is the monomeric staple Au site which shows a small decrease of s-electron counts upon lattice expansion, implying the sensitivity of the staple Au 6s states to the local environment (Figure 3-7).

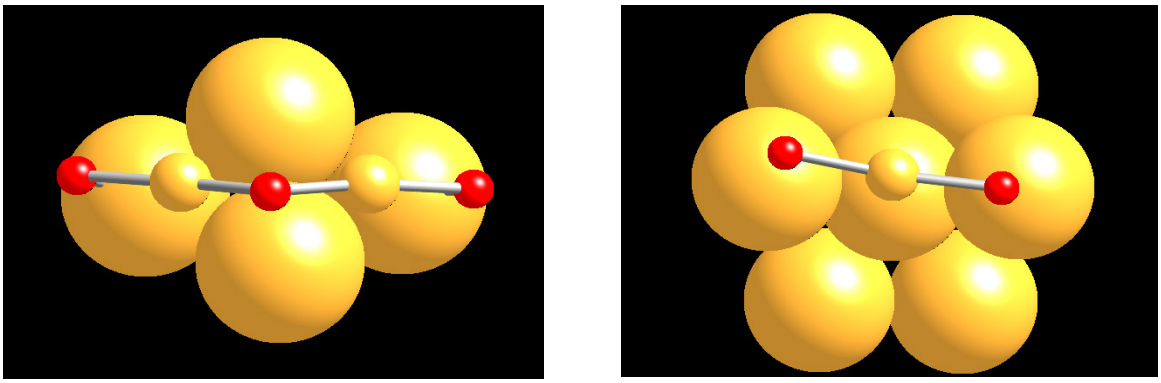

Figure 3-7: An illustration of the difference of local environment of double staple (left) and single staple (right) Au atoms.

Upon 1% bond-expansion of Au_{38}, the low energy side of the d-band shifts towards to Fermi edge, while the high energy side remains essentially unchanged (Figure 3-8). This

causes a narrowing of the overall d-DOS and a small shift of the center of the d-DOS toward the Fermi level (Figure 3-8, part a). Such a narrowing and shifting effect is also observed at each atomic site (Figure 3-8, part b), suggesting the potential tunability of d-electronic behavior of Au at each site via solvation effects. Inspecting the shape of the d-DOS at representative atomic sites indicates that the core Au atom is of metallic nature (widest d-band) and the staple Au is of molecular nature (very sharp d-band). All other Au sites are of metallic nature, but showing significantly narrowed d-bands versus that of the core Au.

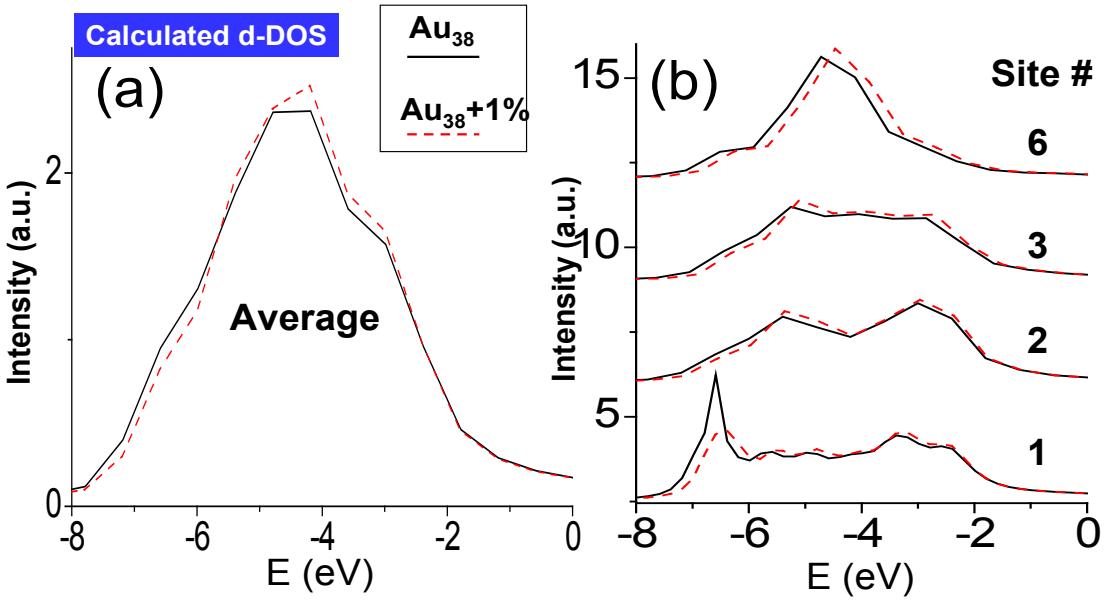

Figure 3-8: Calculations of average (a) and site-specific (b) d-DOS for representative atomic sites of Au_{38} with (---) and without (—) 1% lattice expansion. The 1% lattice expansion was used to simulate the effect of solvation upon the cluster structure. The observed change in d- DOS can be clearly seen for core, bridging, surface and staple environments.

Moreover, a comparison of the d-DOS shape of Au_{38} and Au_{25} shows a narrowing for Au_{25} to a similar-level as in solvated Au_{38}, implying that solvation effects can potentially modify the d-band shape as efficiently as size effects (Figure **3-9**).

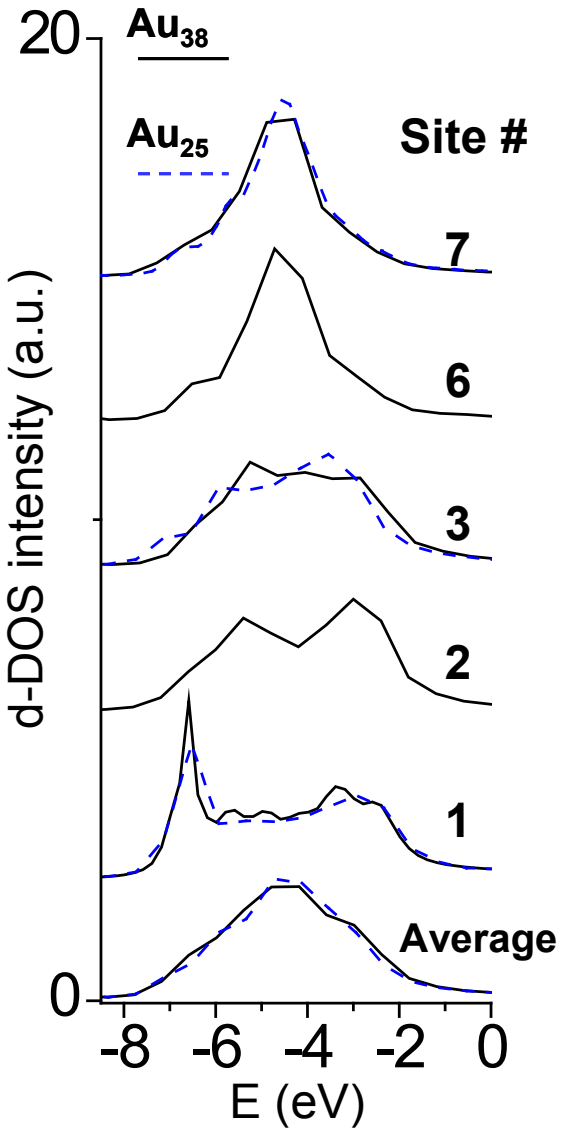

Figure 3-9: Calculated average d-DOS and d-DOS from representative sites in Au_{38} and Au_{25}. For Au_{38}, sites 7 and 8 are the two Au atoms in the same double-staple motif, one near the fusion plane of the biicosahedron Au_{23} core (site 7) and the other far from the fusion plane (site 8).

The solvation-induced change of structure and electronic behavior of Au_{38} reported in this work, albeit of its relatively small extent, has been consistently observed by both experimental and theoretical approaches and should be correlated to the critical dependence of the stability and reactivity of Au_{38} on dispersing solvents.[44] The observed bond expansion and electronic property change presented here is unique for Au-thiolate clusters, presumably due to the extremely high surface-to-volume ratio of Au_{38} (87% Au on surface) and the existence of staple bonding. It is envisioned that by controlling the solvation process of the clusters via selection of the protecting ligand (-SR), solvent and additive solute, more pronounced structural and property changes could possibly be achieved. Remarkably, the change of structure and bonding could potentially influence a variety of other properties such as chemical stability,[72] ferromagnetism[73] and homogeneous catalysis,[48] which are normally sensitive to the variation of electronic behavior of the clusters. Particularly, the predicted d-band shift and narrowing may directly impact the catalytic behavior of transition-metal clusters, which has been found to be very sensitive to Au-Au bond distance and the d-band character.[74] It is also worth noting that the solution-phase XAS technique offers a valuable opportunity to follow these structural and property changes in an *in-situ* manner and it can be extended to S K-edge measurement.

3.5 Conclusion

In conclusion, X-ray absorption spectroscopy studies of the local structure and electronic behavior of solution-phase Au_{38} have been conducted. In addition, *ab initio* calculations of their electronic properties have been presented from a site-specific l-DOS

perspective. This work highlights the importance of solvation effects on the structure and bonding of Au-thiolate clusters and implies the tunablity of their properties by controlling solvation process; it also systematically illustrates the site-specific l-DOS properties of Au_{38} and demonstrates the donation/back-donation Au-S bonding mechanism in the cluster. Furthermore, this work demonstrates the unique potential of XAS in precisely detecting the solution-phase structure and bonding of Au-thiolate clusters, which can be potentially extended to the studies in various dynamic processes in solution.

CHAPTER 4: THE INTERPLAY BETWEEN METALLIC AND MOLECULAR BEHAVIOR IN Au_{25} NANOCLUSTERS

Reproduced with permission from:
MacDonald, M. A.; Chevrie, D.; Zhang, P.; Qian, H.; Jin, R. "The Structure and Bonding of $Au_{25}(SR)_{18}$ from EXAFS: The Interplay of Metallic and Molecular Behavior" *The Journal of Physical Chemistry C,* in press. DOI: 10.1021/jp204922m.

4.1 Introduction

Understanding the atomic structure of gold-thiolate nanoparticles represents an important area of research for both fundamental studies and technological applications of nanotechnology.[2,9] Recent advances in the synthesis and crystallization of ultra-small (<2 nm) gold-thiolate nanoclusters[6,25,49,67] has led to a deeper understanding of the atomic structure of these materials and their resulting structure-property relationships.[21,63,64] However, many questions still exist about the way in which these nanoclusters will behave in complex systems with many external variables, such as temperature,[75] additive solute[45,76] and various dispersing solvents.[44,77] A thorough structural and electronic characterization of the $[TOA]^+[Au_{25}(SCH_2CH_2Ph)_{18}]^{-1}$ nanoparticle has emerged from the literature over recent years.[46,78,79] The well documented and highly symmetric structure of this nanocluster offers a unique opportunity to study the structure of gold-thiolate nanomaterials in different environments to observe how the structure-property relationships of these gold-thiolate nanomaterials are affected by external variables.

To gain further insight into the structure and bonding of these materials, an Au L_3-edge X-ray absorption spectroscopy fine structure (EXAFS) study of the Au-thiolate cluster Au_{25} in solution using both toluene and acetonitrile as solvents, and the solid

phase at low (10 K) and room temperatures (300 K) is presented. The role of solvation effects as well as temperature on the overall structure and behavior of these clusters is discussed.

4.2 Experimental Methods

The synthesis of Au_{25} was conducted by Prof. R. Jin's group at Carnegie Melon University. Details of the synthesis have been reported elsewhere.[22] The Au L_3-edge EXAFS measurements were conducted in transmission mode at the PNC-CAT beamline of the Advance Photon Source at Argonne National Labs in Argonne, IL. A Si (111) monochromator crystal was used in conjunction with a platinum harmonic rejection mirror. For solid-state measurements a toluene solution of Au_{25} was drop-cast onto polyimide (Kapton®) tape and folded until ample signal was observed ($\Delta\mu_0 \approx 0.5\text{-}1.1$). Solution-phase measurements were recorded by dispersing Au_{25} in toluene or acetonitrile in a Teflon sample cell with polyimide windows. Low temperature measurements were conducted using a liquid He cryostat.

Data reduction and refinement was performed using the WinXAS program and standard procedures. Simulation of EXAFS phase and amplitude along with angular momentum density of states (l-DOS) was performed using the FEFF 8 program code[32] and the crystalline structure of Au_{25} previously reported.[21,49]

In the EXAFS refinement S_0^2 was fixed at a value of 0.9 (deduced from the fitting of Au foil) while the *CN* values of different Au-S and Au-Au coordination shells were fixed based upon the crystal structure of Au_{25} (scheme 1). First, a refinement of the FT[$\chi(k)\cdot k^3$] was performed using one Au-S and one Au-Au shell for each sample. Following this all parameters associated with the Au-S bond were fixed and the

refinement of the three Au-Au shells (scheme 1) was performed with correlated E_0 values. This yielded values of R and σ^2 for each shell. All refinements of the FT-EXAFS of Au_{25} were conducted with a k-range of 3-14.5 $Å^{-1}$ for solution phase samples and 3-12 $Å^{-1}$ for solid state samples. An R-range of 1.64-3.06 Å was used in the refinement of the 300 K EXAFS while a range of 1.6-3.3 Å was used for all other spectra. A general error estimate of 0.01 Å was provided for inner shell bond lengths and 0.02 Å for outer shell bond lengths (i.e. $(Au\text{-}Au)_3$).

Simulation of the electronic band occupation was conducted using the l-DOS card FEFF 8. The crystal structure of Au_{25} was used however hydrogen atoms were omitted for simplicity.

For further experimental details please see Appendix A.

4.3 Structure of Au_{25}

A detailed discussion of the structure of Au_{25} has been previously reported in dedicated research articles.[21,49] In general the structure consists of a 13-atom icosahedral Au core (12 surface and 1 central Au) surrounded by six dimeric RS-Au-S(R)-Au-SR staple units (Figure 4-1)

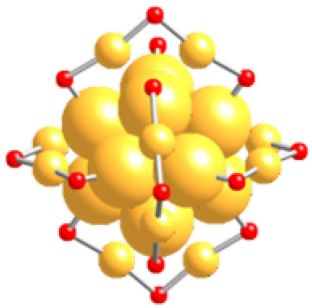

Figure 4-1: Structure of Au_{25} nanocluster.[21] Yellow atoms represent gold while red represents sulfur. Carbon and hydrogen have been omitted for clarity.

These staples are directly anchored to the surface via Au-S bonding while the staple Au atoms have been observed to interact with the icosahedral surface via long range gold-gold bonds. An interesting attribute of Au_{25} for EXAFS analysis is how the structure breaks into several distinct bonding domains (Figure 4-2). The first Au-Au group consists of short bonds (~2.78 Å) between the central Au atom of the icosahedral core and the 12 surface Au atoms, with several short bonds also existing between adjacent surface Au atoms (Figure 4-2, $(Au\text{-}Au)_1$). These six short surface bonds are located directly beneath the apical sulfur of each surface passivating staple unit.

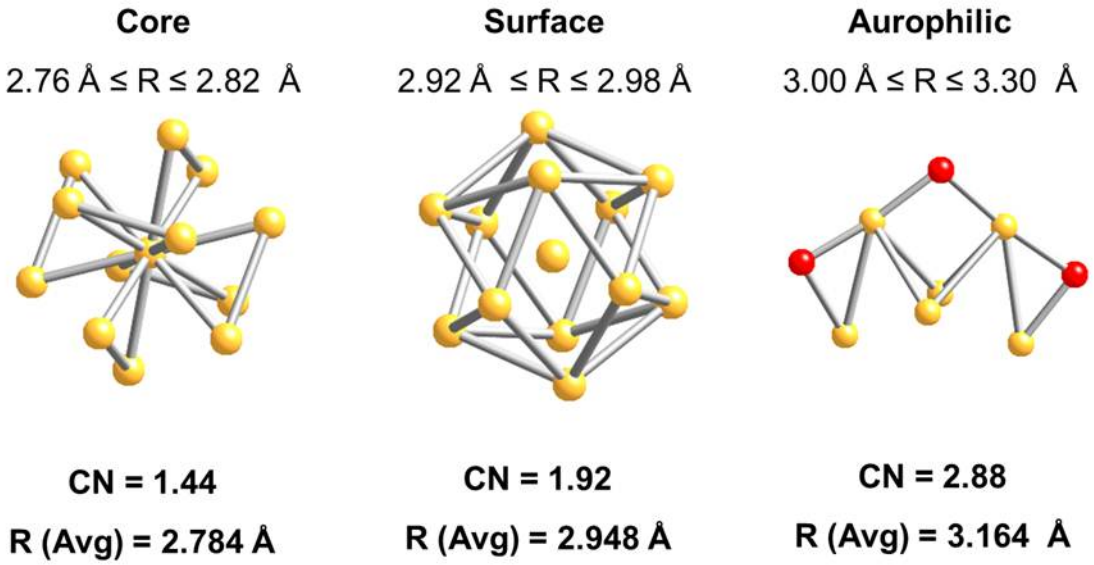

Figure 4-2: Breakdown of bonding in Au_{25} for EXAFS analysis. Average bond lengths and coordination number derived from the crystal structure of Au_{25} are presented for each group.

The second Au-Au shell is composed of mid-length Au-Au bonds (~2.95 Å) located entirely on the surface of the icosahedral core between adjacent surface Au atoms (Figure 4-2, $(Au\text{-}Au)_2$), while the third Au-Au shell, composed of long range (~3.16 Å) surface-staple interactions, exists between staple Au atoms and the icosahedral surface (Figure 4-2, $(Au\text{-}Au)_3$). By following the bonding of Au_{25} via these different groups of bond lengths one can probe the solvation and temperature dependence of the bonding in this cluster from a site specific perspective and gain deeper insight as to the physical properties of this cluster.

4.4 Results

4.4.1 Temperature Dependent Bonding

Table 4-1 summarizes the EXAFS fitting results for Au_{25} in solution and the solid state at room temperature (300 K) and low temperature (10 K). The absolute and imaginary components and their refinements of the Fourier transform of $\chi(k)\cdot k^3$ are shown in Figure 4-3 (a-b).

. In general the EXAFS refinement reveals average bond lengths which are in good agreement with the previously reported crystal structure of Au_{25}.[21,49] The large mean squared displacement (σ^2) for each group of bonds can be attributed both to the distribution of bond lengths within the cluster (static disorder, σ^2_{static}), as well as the low-coordinate bonding environment (dynamic disorder, $\sigma^2_{dynamic}$) which has been shown previously to cause an increase in the mean square displacement of coordination environments.[80] From EXAFS refinement a close comparison of the structural changes which occur upon temperature reduction can be made.

Table 4-1: Structural parameters of Au25 as obtained from EXAFS refinement. The coordination numbers (*CN*) were all fixed using the theoretical values shown in Scheme 1 and one correlated E_0 value was used for all Au-Au paths. The uncertainties of bond distance results are ~0.01 Å for the Au-S, $(Au\text{-}Au)_1$ and $(Au\text{-}Au)_2$ shells and ~0.02 Å for the $(Au\text{-}Au)_3$ shell. The XRD data was collected at 100 K.

Path	Parameter	300 K	10 K	Toluene	ACN	XRD
Au-S	R (Å)	2.32(1)	2.32(1)	2.33(1)	2.32(1)	2.332
	σ^2 (Å^2)	0.0031	0.0020	0.0038	0.0036	-
	E_0 (eV)	-0.5	-0.6	-0.4	-1	-
$(Au\text{-}Au)_1$	R (Å)	2.82(1)	2.80(1)	2.79(1)	2.79(1)	2.784
	σ^2 (Å^2)	0.0084	0.0049	0.0074	0.0072	-
	E_0 (eV)	3.9	4.3	3.7	1.9	-
$(Au\text{-}Au)_2$	R (Å)	2.97(1)	2.97(1)	2.95(1)	2.95(1)	2.948
	σ^2 (Å^2)	0.0224	0.0126	0.0134	0.0146	-
$(Au\text{-}Au)_3$	R (Å)	3.14(2)	3.20(2)	3.19(2)	3.14(2)	3.164
	σ^2 (Å^2)	0.0571	0.0223	0.0326	0.0506	-

In general a decrease in bond length is experienced within the 13-atom icosahedral core of the Au_{25} nanocluster upon temperature reduction. This is accompanied by an apparent increase in the average surface-staple $(Au\text{-}Au)_3$ bond length. It is interesting to note the large effect of temperature on the mean squared displacement for the $(Au\text{-}Au)_3$ bonds compared to the other groups (i.e. ~65% reduction in σ^2 for $(Au\text{-}Au)_3$ versus ~35% for all other groups). This suggests a stronger contribution to the overall σ^2 of the $(Au\text{-}Au)_3$ bonds from dynamic disorder versus the other groups and suggests a weak surface-staple interaction due to the high $Au_{surface}$-Au_{staple} dynamic disorder.

Previous studies on the temperature-dependent bonding of both bulk gold and gold-thiolate nanoparticles have shown that a contraction of the lattice should be expected with temperature decrease.[81,82] Indeed this is not uncommon behavior for metallic nanoparticle systems, with only a few examples of negative or zero thermal expansion having been reported among supported metal nanoparticles.[75,81,83,84] What is interesting to note, however, is the differing thermal behavior of the metallic icosahedral core of the Au_{25} nanoparticle and the surrounding gold-thiolate staple system. Interestingly, the more "molecular" S-Au-S-Au-S staple system demonstrates significantly less response to the temperature change than the "metallic" 13-atom core. It has been proposed recently that bonding interactions exist between the surface and staple Au sites and are essential to the robustness of these materials.[72,85,86]

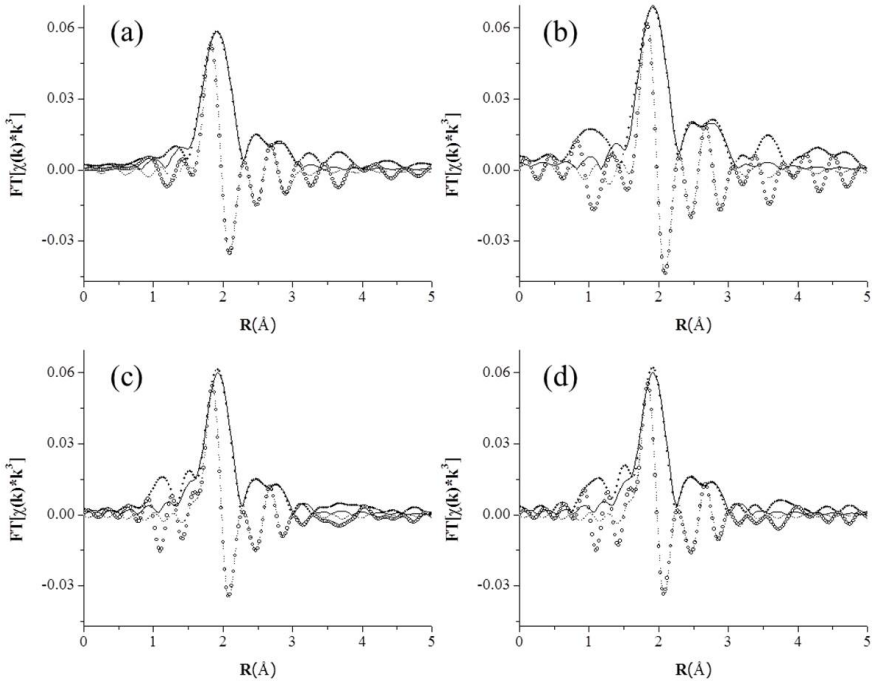

Figure 4-3: Absolute (■) and imaginary (○) components and refinement of the absolute (—) and imaginary (---) components of the FT[$\chi(k)*k^3$] EXAFS of Au_{25}. The spectra represent (a) solid state structure at 300 K, (b) solid state structure at 10 K, (c) toluene-solvated structure at 300 K and (d) acetonitrile-solvated structure at 300 K.

The lack of thermal contraction of the staple Au could then be due to several reasons. One possibility could be associated with the local atomic environment of the staple Au. Whereas Au-complexes typically maintain S-Au-S bond angles of ~180°, the cost of distorting this approximately linear S-Au-S geometry versus the gain in Au-Au bonding with the Au_{13} surface may not be worthwhile.[28] Another possible reason for the differing thermal behavior could be associated with the R-group of the thiol ligand. Crystallographic data have shown that in the solid state the aromatic units of phenylethanethiol group together to accommodate π-π interactions in the surrounding ligand network of the nanocluster[21,49] (Figure 4-4). As a result it is plausible that it is the hardness of these aromatic ligand tail interactions that prevent the staple systems from contracting with the relatively soft Au_{13} core, rather than the local electronic environment of the staple Au (i.e., Au-S-Au and/or S-Au-S bond angle).

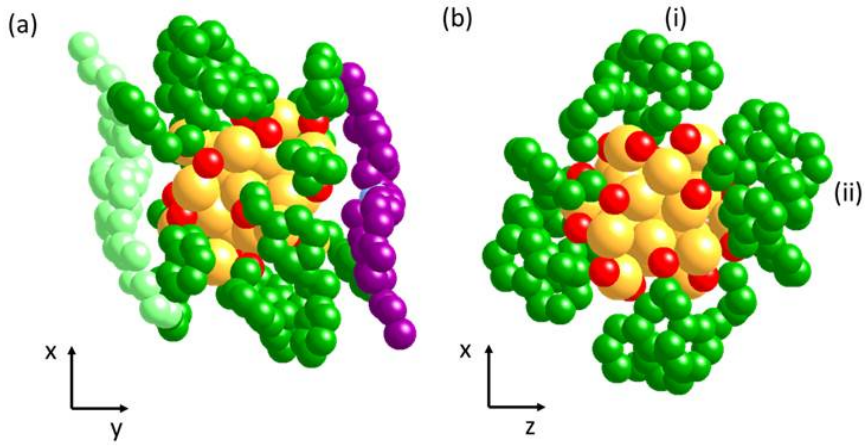

Figure 4-4: Space filling model of the solid-state structure of (a) $Au_{25}(SCH_2CH_2Ph)_{18}^{-1}$ with the TOA^+ cation illustrating how accommodation of the bulky cation causes a displacement of the ligand tails, and (b) how the ligand tails group together to accommodate π-π interactions, marked by (i) and (ii). Yellow, red and dark green represent gold, sulfur and ligand carbon atoms. Blue, light green and purple represent the nitrogen, and carbon atoms of the TOA^+ cations surrounding Au_{25}^-. Hydrogen atoms have been omitted for clarity.

While the scale of change observed in this study is quite modest, it is possible that the site-specific nature of this behavior could utilized in the design of future metal nanomaterials. Previous studies have demonstrated that both chemical and optical behavior can be attributed to local atomic environments in Au_{25} and other nanoclusters.[21,72,87] It will be interesting to see if this differing behavior between the metallic core and molecular staple systems can potentially be exploited to achieve new stable mono- or multi-metallic nanocluster systems by balancing different metal-metal (core-surface and surface-staple), metal-ligand (ligand-surface and ligand-staple) and ligand-ligand (tailgroup-tailgroup) interactions.[85,86,88,89]

4.4.2 Solvation Dependent Bonding

A critical question in nanoscience pertains to the structure of nanomaterials in their applied environment. While solid-state structures of nanomaterials are invaluable in the information they provide, ultimately the synthesis and applications of these materials occur in a solvated environment. To gain further insight into the interplay of the metallic and molecular portions of Au_{25} a comparison of the structure of Au_{25} solvated in toluene and acetonitrile to the solid state structure at 300 K (Table 4-1) is made. The absolute and imaginary components and their refinements of the Fourier transform of $\chi(k)\cdot k^3$ are shown in Figure 4-3 (c-d).

From the comparison a general decrease in the bond length of the Au_{13} core ($(Au\text{-}Au)_1$, $(Au\text{-}Au)_2$) is observed with an accompanying increase in the $(Au\text{-}Au)_3$ bond length of the cluster when solvated in toluene (Figure 4-5). This trend is the same as what was observed in the temperature dependent study (see discussions above), however, while in

the temperature dependent study the observed structural changes of the nanomaterial can be rationalized by the metallic nature of the cluster core, in this scenario the observed structural change is purely a result of solvation.

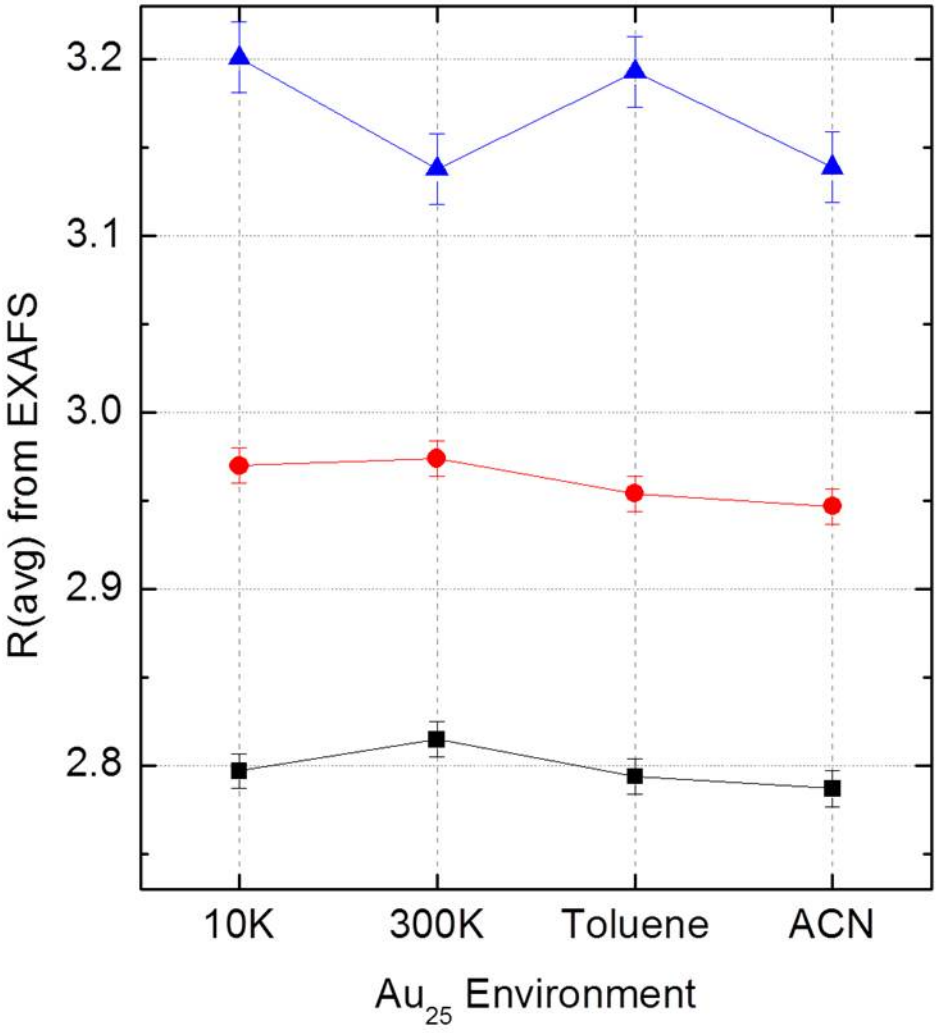

Figure 4-5: Experimentally determine bond length of $(Au\text{-}Au)_1$ (■), $(Au\text{-}Au)_2$ (●) and $(Au\text{-}Au)_3$ (▲) for Au_{25} at 10 K, 300 K, solvated in toluene and solvated in acetonitrile. All bond lengths were extracted from refinement of the FT[$\chi(k)*k^3$] EXAFS spectra.

As mentioned above, the solid state structure of anionic Au_{25} (counterion: TOA^+) shows that in the solid state the aromatic tails of the phenylethanethiol ligands of Au_{25} organize into groups to facilitate π-π bonding, cation-π bonding as well as to accompany the bulky tetraoctylammonium cation into the solid state structure[49] (Figure 4-4). Indeed, it has been reported that the binding strength of aromatic π-π stacking is significantly weakened upon solvation in an apolar aromatic solvent due to the favorable interaction between the solvent molecules and the π-stacking system.[90] Upon solvation of Au_{25} in an aromatic solvent like toluene, it is plausible that interactions of the ligand tailgroup with the aromatic solvent molecules facilitate Au_{25} to adopt a slightly different, more favorable geometry. This idea is supported by the general decrease in the mean squared displacement (σ^2) of the $(Au\text{-}Au)_3$ bond length observed upon cluster solvation in toluene (Figure 4-6, Table 4-1).

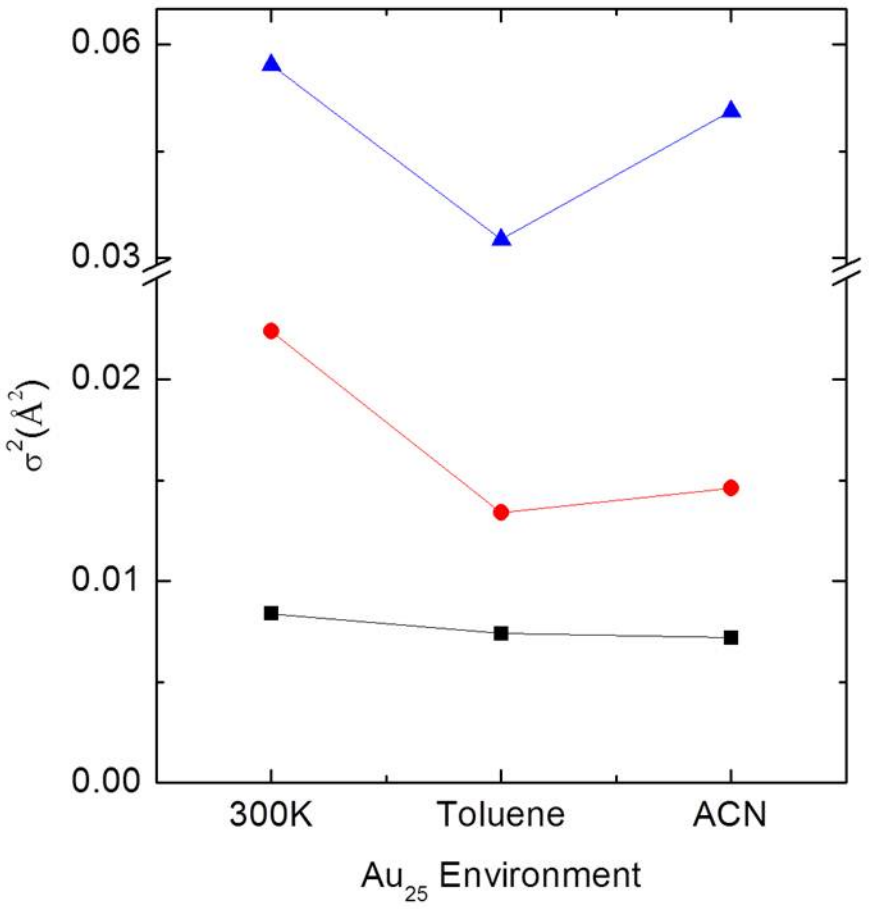

Figure 4-6: Experimentally determine mean squared displacement of $(Au\text{-}Au)_1$(■), $(Au\text{-}Au)_2$ (●) and $(Au\text{-}Au)_3$ (▲) for Au_{25} at 300 K in the solid state, solvated in toluene and solvated in acetonitrile. All bond lengths were extracted from refinement of the FT[$\chi(k)*k^3$] EXAFS spectra.

Whereas these comparisons were conducted at constant temperature this suggests less static disorder in this group of $(Au\text{-}Au)_3$ bonds upon solvation. This idea is also supported by the solid state structure of the neutral form of Au_{25} previously reported.[91] In the crystal structure of the neutral Au_{25} cluster the bulky tetraoctylammonium cation is absent. As a result the ligand tailgroups surrounding Au_{25} are found to adopt a different conformation than in the anionic form of Au_{25} and the distribution of Au-Au bond lengths in the structure is different (Figure 4-7).

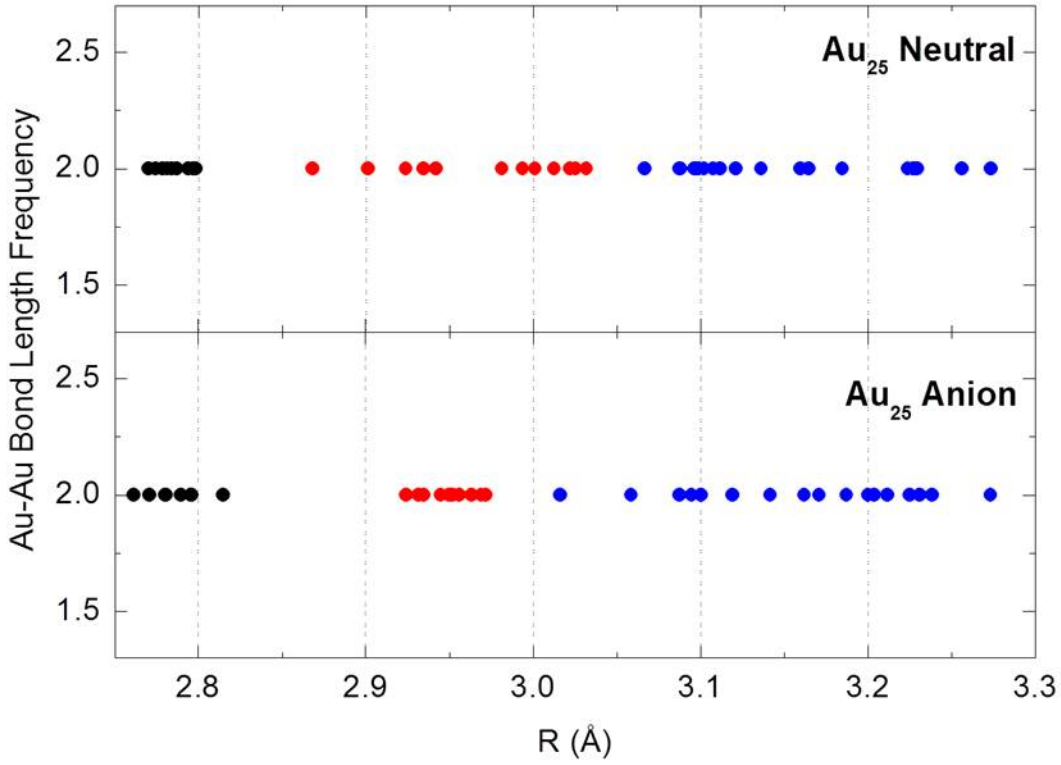

Figure 4-7: Distribution of $(Au\text{-}Au)_1$(●), $(Au\text{-}Au)_2$ (●) and $(Au\text{-}Au)_3$ (●) bond lengths within the Au_{25} cluster. The changes in bonding are most likely attributable to the absence of the TOA^+ cation in the unit cell of the neutral Au_{25}. The spread of the bond lengths in each group effects the observed mean square displacements in EXAFS refinement. Bond length data was collected from literature reference.[21,91]

It is interesting to contrast the behavior of Au_{25} and that of the closely related Au_{38} structure upon solvation in toluene. It has been previously observed that upon solvation Au_{38} experience a general increase in bond length throughout the cluster.[77] This differing behavior can possibly be attributed to several factors. First, whereas Au_{38} exists in the neutral charge state it does not need to accommodate a counter ion into the solid-state packing structure. As a result the bonding in the solid-state of Au_{38} may have less ligand-induced strain then Au_{25} and thus lead to a different solvation-induced structural change. This is somewhat supported by considering the differing structural disorder within the

structure of the neutral Au_{25} cluster when compared to the anionic cluster. In addition, the neutral charge state of Au_{38} will make the cluster inherently more hydrophilic and thus may further influence the interaction between the cluster and the solvent. Whereas Au_{25} exists as an anion the ligand behavior may be influenced by this formal electrostatic charge. A detailed comparison of the solvation behavior of Au_{25} and Au_{38} is difficult to make, however, due to the larger degree of structural disorder in Au_{38}. This makes analyzing the solvation behavior from a site-specific perspective much more difficult than with Au_{25}.

Comparing the solvation effect of acetonitrile on Au_{25} a more pronounced decrease in bond length is observed within the Au_{13} core ($(Au\text{-}Au)_1$ and $(Au\text{-}Au)_2$ shells) relative to the toluene system, however, following solvation the $(Au\text{-}Au)_3$ bond lengths stay approximately the same (Figure 4-5, Table 4-1). Polar solvents like acetonitrile lack any kind of aromatic organic structural unit one possible explanation for the differing solvated structure could arise from an inability of acetonitrile to disrupt the π-π interactions of the ligand shell[90] and as a result the ligand-induced strain on the nanocluster is not reduced as effectively as with toluene. This could potentially explain the smaller reduction in the $(Au\text{-}Au)_3$ mean square displacement observed when dispersed in acetonitrile (Figure 4-6, Table 4-1). As a result of the different interactions of the ligand tailgroups of Au_{25} and the nonaromatic dispersing solvent, slightly different structural properties are observed within the cluster.

Whereas acetonitrile represents a Lewis basic solvent it seems reasonable that coordination to the Au_{25} surface could also be possible upon solvation. Indeed this idea develops relatively intuitively because Lewis basic nitrogen moieties (amine, cyanide,

etc…) have been known to have a high affinity for coordinating to gold.[2] It appears that as a result of interaction with the solvent, an electronic interaction could take place which causes the Au_{13} core to contract while leaving the ligand shell, and thus the $(Au\text{-}Au)_3$ bond length, relatively unaffected. What is interesting, however, is the observation that acetonitrile is interacting with the relatively "metallic" Au_{13} cluster core directly, rather than the "molecular" staple Au. A reason for this may follow from the consideration of the electronic properties of these two Au environments.

It has been shown previously that the Au atoms in the Au_{102} nanocluster exhibit different electronic distributions about each coordination environment, that is, the Au atoms of the staple sites in Au_{102} exhibit a higher occupation of their sp-band versus their core-Au counterparts.[72] This change in electronic character is rationalized as a direct result of the local bonding topology of the system. It has also been shown that amine molecules interact with gold through a donation of their lone-pair electrons into the Au 6s orbital in single molecular junctions.[92] Extending this rationale to Au_{25} it seems reasonable to observe preferential interaction of acetonitrile with the available unoccupied s-states of the Au_{13} core rather than the Au staple sites due to the higher density of unoccupied s-states of the core. Figure 4-8 illustrates the anti-correlated s-d electron density of Au_{25} from a site specific perspective. This picture is consistent with previous DFT calculations which predict a largely sp-character LUMO composed primarily of Au core atomic orbital character.[21] This differing local electronic character is interesting and it could help to explain other physical and chemical properties of these nanoclusters such as catalytic activity, from a site specific perspective.

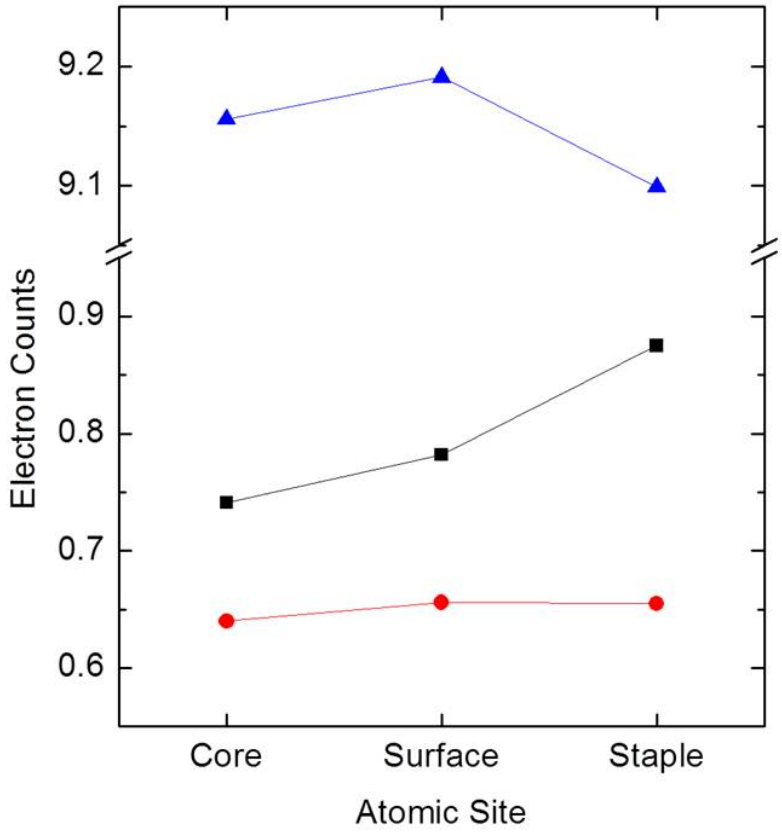

Figure 4-8: Site specific l-DOS electron counts of 6s- (■), 6p- (●), and 5d- (▲) electrons in Au_{25} calculated using FEFF 8. The anti-correlated s-d electron distribution gives rise to different local properties.

4.5 Conclusion

In conclusion, the structure and bonding of Au_{25} nanoclusters has been examined under different external environmental conditions such as temperature, and dispersing solvent, from a site-specific perspective via EXAFS. The structural changes observed for Au_{25} help to illustrate the interplay of local bonding environments upon the overall physical and chemical properties of this nanocluster. This study will aid in developing a deeper understanding of the structure-property relationships of these and other nanomaterials and the tunability of their behavior in solution phase processes.

CHAPTER 5: OVERALL CONCLUSIONS

In conclusion, the site- and size-dependence of the structure and electronic properties of truly monodisperse gold-thiolate nanoclusters have been observed from X-ray spectroscopy. The observed structural changes presented throughout this work have been accounted for by complementary *ab initio* calculations of electronic properties.

Firstly, the atomic structure of Au_{144} has been illustrated from XANES, EXAFS and XPS, and a high-precision; atomic-site-specific illustration of its bonding has been presented. The structure of Au_{144} is found to be in good agreement with the recently reported theoretical model. By extending the X-ray studies to smaller nanoparticles, the size-dependent increase of Au s-/d-DOS is observed via Au L_{III}-edge XANES and S K-edge NEXAFS.

Next, the solution-phase structure of Au_{38} nanoclusters via X-ray absorption spectroscopy has been reported. A significant bond expansion associated with an increase of Au d-electron DOS have been observed upon solvation of Au_{38} in toluene. These findings are accounted for by projected DOS calculations, which further illustrate the unique electronic behavior of Au_{38} from a site-specific perspective.

Additionally, the structure and bonding of Au_{25} nanoclusters have been examined under different external environmental conditions such as low temperature, and dispersing solvent. Differing behavior between the surface staple Au sites and core metal sites in response to solvation and temperature has been observed. A mechanism for the observed dependence of these changes upon the ligand tail, solvent and solid-phase structure is proposed. The structural changes observed for Au_{25} illustrate the interplay of

local bonding environments upon the overall physical and chemical properties of this nanocluster.

Finally, this work has shown that X-ray spectroscopies, including XANES, EXAFS and XPS, are powerful tools for studying the structure and electronic properties of compositionally precise nanoclusters. When these tools are combined with *ab initio* calculations a detailed and systematic illustration of the bonding of properties may be achieved, helping to overcome many of the challenges of modern nanomaterials characterization. The methods and results presented within this work will find potential application in the design of future gold-thiolate nanocluster based catalysts and electronic devices.

REFERENCES

(1) Ozin, G. A. *Adv. Mater.* **1992**, *4*, 612.
(2) Daniel, M. C.; Astruc, D. *Chem. Rev.* **2004**, *104*, 293.
(3) Kelly, K. L.; Coronado, E.; Zhao, L. L.; Schatz, G. C. *J. Phys. Chem. B* **2003**, *107*, 668.
(4) Laurent, S.; Forge, D.; Port, M.; Roch, A.; Robic, C.; Vander Elst, L.; Muller, R. N. *Chem. Rev.* **2008**, *108*, 2064.
(5) Aiken, J. D.; Finke, R. G. *Journal Of Molecular Catalysis A-Chemical* **1999**, *145*, 1.
(6) Adzic, R. R.; Zhang, J.; Sasaki, K.; Vukmirovic, M. B.; Shao, M.; Wang, J. X.; Nilekar, A. U.; Mavrikakis, M.; Valerio, J. A.; Uribe, F. *Topics In Catalysis* **2007**, *46*, 249.
(7) Haruta, M.; Date, M. *Appl. Catal. A* **2001**, *222*, 427.
(8) Toshima, N.; Yonezawa, T. *New J. Chem.* **1998**, *22*, 1179.
(9) Whetten, R. L.; Khoury, J. T.; Alvarez, M. M.; Murthy, S.; Vezmar, I.; Wang, Z. L.; Stephens, P. W.; Cleveland, C. L.; Luedtke, W. D.; Landman, U. *Adv. Mater.* **1996**, *8*, 428.
(10) Templeton, A. C.; Wuelfing, M. P.; Murray, R. W. *Acc. Chem. Res.* **2000**, *33*, 27.
(11) Brust, M.; Walker, M.; Bethell, D.; Schiffrin, D. J.; Whyman, R. *J. Chem. Soc. Chem. Comm.* **1994**, 801.
(12) Brust, M.; Fink, J.; Bethell, D.; Schiffrin, D. J.; Kiely, C. *J. Chem. Soc. Chem. Comm.* **1995**, 1655.
(13) Elghanian, R.; Storhoff, J. J.; Mucic, R. C.; Letsinger, R. L.; Mirkin, C. A. *Science* **1997**, *277*, 1078.
(14) Rosi, N. L.; Mirkin, C. A. *Chem. Rev.* **2005**, *105*, 1547.
(15) Paciotti, G. F.; Myer, L.; Weinreich, D.; Goia, D.; Pavel, N.; McLaughlin, R. E.; Tamarkin, L. *Drug Delivery* **2004**, *11*, 169.
(16) Liu, C. L.; Ho, M. L.; Chen, Y. C.; Hsieh, C. C.; Lin, Y. C.; Wang, Y. H.; Yang, M. J.; Duan, H. S.; Chen, B. S.; Lee, J. F.; Hsiao, J. K.; Chou, P. T. *J. Phys. Chem. C* **2009**, *113*, 21082.
(17) Schaaff, T. G.; Shafigullin, M. N.; Khoury, J. T.; Vezmar, I.; Whetten, R. L. *J. Phys. Chem. B* **2001**, *105*, 8785.
(18) Negishi, Y.; Takasugi, Y.; Sato, S.; Yao, H.; Kimura, K.; Tsukuda, T. *J. Am. Chem. Soc.* **2004**, *126*, 6518.
(19) Jin, R. C. *Nanoscale* **2010**, *2*, 343.
(20) Qian, H. F.; Jin, R. C. *Nano Letters* **2009**, *9*, 4083.
(21) Zhu, M.; Aikens, C. M.; Hollander, F. J.; Schatz, G. C.; Jin, R. *J. Am. Chem. Soc.* **2008**, *130*, 5883.
(22) Zhu, M.; Lanni, E.; Garg, N.; Bier, M. E.; Jin, R. *J. Am. Chem. Soc.* **2008**, *130*, 1138.
(23) Wu, Z. K.; Lanni, E.; Chen, W. Q.; Bier, M. E.; Ly, D.; Jin, R. C. *J. Am. Chem. Soc.* **2009**, *131*, 16672.

(24) Shichibu, Y.; Negishi, Y.; Tsukuda, T.; Teranishi, T. *J. Am. Chem. Soc.* **2005**, *127*, 13464.
(25) Jadzinsky, P. D.; Calero, G.; Ackerson, C. J.; Bushnell, D. A.; Kornberg, R. D. *Science* **2007**, *318*, 430.
(26) Petroski, J.; Chou, M.; Creutz, C. *J. Organomet. Chem.* **2009**, *694*, 1138.
(27) Jiang, D. E.; Tiago, M. L.; Luo, W. D.; Dai, S. *J. Am. Chem. Soc.* **2008**, *130*, 2777.
(28) Schmidbaur, H.; Schier, A. *Chem. Soc. Rev.* **2008**, *37*, 1931.
(29) Qian, H. F.; Zhu, Y.; Jin, R. C. *Acs Nano* **2009**, *3*, 3795.
(30) *X-ray Absorption: Principles, Applications, Techniques of EXAFS, SEXAFS, and XANES*; Koningsberger, D. C., Prins, R., Ed.; John Wiley & Sons: Toronto, 1988; Vol. 92.
(31) Bunker, G. *Introduction to XAFS: A Practical Guide to X-ray Absorption Fine Structure Spectroscopy*; Cambridge University Press: Cambridge, 2010.
(32) Rehr, J. J.; Albers, R. C. *Rev. Mod. Phys.* **2000**, *72*, 621.
(33) Sham, T. K. *Phys. Rev. B* **1985**, *31*, 1888.
(34) Ankudinov, A. L.; Ravel, B.; Rehr, J. J.; Conradson, S. D. *Phys. Rev. B* **1998**, *58*, 7565.
(35) Nardelli, A.; Fronzoni, G.; Stener, M. *J. Phys. Chem. C* **2009**, *113*, 14844.
(36) Kruger, S.; Stener, M.; Mayer, M.; Nortemann, F.; Rosch, N. *Theochem-J. Mol. Struct.* **2000**, *527*, 63.
(37) Rehr, J. J.; Kas, J. J.; Prange, M. P.; Sorini, A. P.; Takimoto, Y.; Vila, F. *C. R. Phys.* **2009**, *10*, 548.
(38) Rehr, J. J.; Deleon, J. M.; Zabinsky, S. I.; Albers, R. C. *J. Am. Chem. Soc.* **1991**, *113*, 5135.
(39) Rehr, J. J.; Albers, R. C. *Phys. Rev. B* **1990**, *41*, 8139.
(40) Negishi, Y.; Nobusada, K.; Tsukuda, T. *J. Am. Chem. Soc.* **2005**, *127*, 5261.
(41) Toikkanen, O.; Ruiz, V.; Ronholm, G.; Kalkkinen, N.; Liljeroth, P.; Quinn, B. M. *J. Am. Chem. Soc.* **2008**, *130*, 11049.
(42) Dharmaratne, A. C.; Krick, T.; Dass, A. *J. Am. Chem. Soc.* **2009**, *131*, 13604.
(43) Wu, Z. W.; Gayathri, C.; Gil, R. R.; Jin, R. C. *J. Am. Chem. Soc.* **2009**, *131*, 6535.
(44) Toikkanen, O.; Carlsson, S.; Dass, A.; RoÌˆnnholm, G.; Kalkkinen, N.; Quinn, B. M. *J. Phys. Chem. Lett.* **2009**, *1*, 32.
(45) Shichibu, Y.; Negishi, Y.; Tsunoyama, H.; Kanehara, M.; Teranishi, T.; Tsukuda, T. *Small* **2007**, *3*, 835.
(46) Wu, Z. K.; Jin, R. C. *Acs Nano* **2009**, *3*, 2036.
(47) Yan, Z.; Huifeng, Q.; Bethany A., D.; Rongchao, J. *Angew. Chem. Int. Ed.* **2010**, *49*, 1295.
(48) Zhu, Y.; Qian, H.; Zhu, M.; Jin, R. *Adv. Mater.* **2010**, *22*, 1915.
(49) Heaven, M. W.; Dass, A.; White, P. S.; Holt, K. M.; Murray, R. W. *J. Am. Chem. Soc.* **2008**, *130*, 3754.

(50) Lopez-Acevedo, O.; Akola, J.; Whetten, R. L.; Gronbeck, H.; Hakkinen, H. *J. Phys. Chem. C* **2009**, *113*, 5035.
(51) Simms, G. A.; Padmos, J. D.; Zhang, P. *J. Chem. Phys.* **2009**, *131*, 214703.
(52) Zanchet, D.; Tolentino, H.; Alves, M. C. M.; Alves, O. L.; Ugarte, D. *Chem. Phys. Lett.* **2000**, *323*, 167.
(53) Leung, B. O.; Jalilehvand, F.; Szilagyi, R. K. *J. Phys. Chem. B* **2008**, *112*, 4770.
(54) Zhang, P.; Sham, T. K. *Phys. Rev. Lett.* **2003**, *90*, 245502.
(55) Bourg, M. C.; Badia, A.; Lennox, R. B. *J. Phys. Chem. B* **2000**, *104*, 6562.
(56) Walter, M.; Akola, J.; Lopez-Acevedo, O.; Jadzinsky, P. D.; Calero, G.; Ackerson, C. J.; Whetten, R. L.; Gronbeck, H.; Hakkinen, H. *Proc. Natl. Acad. Sci. U. S. A.* **2008**, *105*, 9157.
(57) Taylor, K. J.; Pettiettehall, C. L.; Cheshnovsky, O.; Smalley, R. E. *J. Chem. Phys.* **1992**, *96*, 3319.
(58) Glaser, T.; Hedman, B.; Hodgson, K. O.; Solomon, E. I. *Acc. Chem. Res.* **2000**, *33*, 859.
(59) Jalilehvand, F. *Chem. Soc. Rev.* **2006**, *35*, 1256.
(60) Chaudhuri, A.; Odelius, M.; Jones, R. G.; Lee, T. L.; Detlefs, B.; Woodruff, D. P. *J. Chem. Phys.* **2009**, *130*, 124708.
(61) Di Felice, R.; Selloni, A.; Molinari, E. *J. Phys. Chem. B* **2003**, *107*, 1151.
(62) Pei, Y.; Gao, Y.; Zeng, X. C. *J. Am. Chem. Soc.* **2008**, *130*, 7830.
(63) Lopez-Acevedo, O.; Tsunoyama, H.; Tsukuda, T.; HaÌˆkkinen, H.; Aikens, C. M. *J. Am. Chem. Soc.*, *132*, 8210.
(64) MacDonald, M. A.; Zhang, P.; Qian, H.; Jin, R. *The Journal of Physical Chemistry Letters* **2010**, 1821.
(65) Chen, S.; Ingram, R. S.; Hostetler, M. J.; Pietron, J. J.; Murray, R. W.; Schaaff, T. G.; Khoury, J. T.; Alvarez, M. M.; Whetten, R. L. *Science* **1998**, *280*, 2098.
(66) Ressler, T. *Journal Of Synchrotron Radiation* **1998**, *5*, 118.
(67) Qian, H.; Eckenhoff, W. T.; Zhu, Y.; Pintauer, T.; Jin, R. *J. Am. Chem. Soc.* **2010**, *132*, 8280.
(68) Sham, T. K.; Kim, P. S. G.; Zhang, P. *Solid State Commun.* **2006**, *138*, 553.
(69) Aakesson, R.; Persson, I.; Sandstroem, M.; Wahlgren, U. *Inorg. Chem.* **1994**, *33*, 3715.
(70) van Bokhoven, J. A.; Miller, J. T. *The Journal of Physical Chemistry C* **2007**, *111*, 9245.
(71) Park, Y. S.; Whalley, A. C.; Kamenetska, M.; Steigerwald, M. L.; Hybertsen, M. S.; Nuckolls, C.; Venkataraman, L. *J. Am. Chem. Soc.* **2007**, *129*, 15768.
(72) Reimers, J. R.; Wang, Y.; Cankurtaran, B. O.; Ford, M. J. *J. Am. Chem. Soc.* **2010**, *132*, 8378.
(73) Negishi, Y.; Tsunoyama, H.; Suzuki, M.; Kawamura, N.; Matsushita, M. M.; Maruyama, K.; Sugawara, T.; Yokoyama, T.; Tsukuda, T. *J. Am. Chem. Soc.* **2006**, *128*, 12034.

(74) Miller, J. T.; Kropf, A. J.; Zha, Y.; Regalbuto, J. R.; Delannoy, L.; Louis, C.; Bus, E.; van Bokhoven, J. A. *J. Catal.* **2006**, *240*, 222.
(75) Sanchez, S. I.; Menard, L. D.; Bram, A.; Kang, J. H.; Small, M. W.; Nuzzo, R. G.; Frenkel, A. I. *J. Am. Chem. Soc.* **2009**, *131*, 7040.
(76) Zhu, M.; Chan, G.; Qian, H.; Jin, R. *Nanoscale* **2011**, *3*, 1703.
(77) MacDonald, M. A.; Zhang, P.; Chen, N.; Qian, H.; Jin, R. *The Journal of Physical Chemistry C* **2011**, *115*, 65.
(78) Parker, J. F.; Fields-Zinna, C. A.; Murray, R. W. *Acc. Chem. Res.* **2010**, *43*, 1289.
(79) Akola, J.; Walter, M.; Whetten, R. L.; Hakkinen, H.; Gronbeck, H. *J. Am. Chem. Soc.* **2008**, *130*, 3756.
(80) Guliamov, O.; Frenkel, A. I.; Menard, L. D.; Nuzzo, R. G.; Kronik, L. *J. Am. Chem. Soc.* **2007**, *129*, 10978.
(81) Comaschi, T.; Balerna, A.; Mobilio, S. *Phys. Rev. B* **2008**, *77*, 075432.
(82) Comaschi, T.; Balerna, A.; Mobilio, S. *Journal Of Physics-Condensed Matter* **2009**, *21*.
(83) Cuenya, B. R.; Frenkel, A. I.; Mostafa, S.; Behafarid, F.; Croy, J. R.; Ono, L. K.; Wang, Q. *Phys. Rev. B* **2010**, *82*.
(84) Kang, J. H.; Menard, L. D.; Nuzzo, R. G.; Frenkel, A. I. *J. Am. Chem. Soc.* **2006**, *128*, 12068.
(85) Femoni, C.; Iapalucci, M. C.; Longoni, G.; Zacchini, S.; Zarra, S. *J. Am. Chem. Soc.* **2011**, *133*, 2406.
(86) Jung, J.; Kim, H.; Han, Y.-K. *J. Am. Chem. Soc.* **2011**, *133*, 6090.
(87) Yan, Z.; Huifeng, Q.; Bethany , A. D.; Rongchao, J. *Angewandte Chemie International Edition*, *49*, 1295.
(88) Dong, R.; Chen, X.; Zhao, H.; Wang, X.; Shu, H.; Ding, Z.; Wei, L. *Phys. Chem. Chem. Phys.* **2011**, *13*, 3274.
(89) Femoni, C.; Iapalucci, M. C.; Longoni, G.; Tiozzo, C.; Zacchini, S. *Angewandte Chemie International Edition* **2008**, *47*, 6666.
(90) Smithrud, D. B.; Diederich, F. *J. Am. Chem. Soc.* **1990**, *112*, 339.
(91) Zhu, M. Z.; Eckenhoff, W. T.; Pintauer, T.; Jin, R. C. *J. Phys. Chem. C* **2008**, *112*, 14221.
(92) Venkataraman, L.; Klare, J. E.; Tam, I. W.; Nuckolls, C.; Hybertsen, M. S.; Steigerwald, M. L. *Nano Letters* **2006**, *6*, 458.

APPENDIX A: EXPERIMENTAL NOTES

A.1. Beamline-specific Experimental Details:

HXMA: All experiments were conducted in an air atmosphere at the HXMA beamline using a Si (111) monochromator crystal, Rh mirrors and three ion chambers (15 cm, 30 cm, 30cm) filled with a N_2/Ar gas mixture. The samples were loaded into a Teflon sample cell.

SXRMB: Samples dried onto Si(111) wafers or spread onto carbon tape and loaded into the vacuum chamber for analysis. Spectra were collected using both Si (111) and InSb (111) monochromator crystals for NEXAFS and EXAFS respectively. The vacuum chamber was typically run at a base pressure of approximately 10^{-7} torr

SGM: Photoemission experiments were conducted in the Scienta endstations of the SGM beamline. Colloidal solutions of the samples were either dried on Si(111) wafers or powdered samples were spread on carbon tape and mounted for analysis.

PGM: Experiments at the PGM beamline were conducted simultaneously in fluorescence and total electron yields. Samples were spread on carbon tape and loaded into the sample chamber for analysis.

A.2. Notes on collecting EXAFS of gold nanoclusters:

Refining the fine structure of gold-thiolate nanoclusters is particularly challenging due to the low coordinate environment of the Au atoms, and the high degree of structural

disorder within the cluster. These two effects combine to give a small value of N, and large value of σ^2 thus reducing the amplitude of the EXAFS signal greatly. To overcome this it is essential to take care in sample preparation. In particular liquid-phase sample preparation has proven quite beneficial for preparing a completely homogeneous sample. This route, however, requires that there be ample sample to create a solution that is concentrated enough to provide good EXAFS. In addition, the ability of the solvent to attenuate X-rays, as well as the compatibility of the solvent and the sample cell are all important considerations. Normally non-substituted organic solvents (i.e. toluene, hexanes, acetonitrile) are suitable for liquid phase EXAFS, however solvents with heavy substituents (dichloromethane) and water will more heavily attenuate the X-ray beam.

For solid-state samples it is often sufficient to spread the sample on an adhesive tape and fold the tape until ample signal is observed. However, if the sample must be recovered following the experiment without contamination from the tape adhesive it may be better to prepare a thin film of the sample on a polymer film. In this case the dispersing solvent should be chosen to give a good compromise between the solubility of the product and the vapor pressure of the solvent. The faster the solvent evaporates the more homogenous the resulting film.

A.3. Notes on collecting XPS of gold nanoclusters:

The sampling depth via XPS is usually reported to be ~3 mean free path lengths, thus it is ideal for the study of gold-thiolate nanoclusters because this value is usually greater than the overall dimensions of the clusters. Care should be taken, however, to ensure beam caused damage does not occur (Figure B - 1). This generally occurs due to

heating due to the X-ray beam. Whereas these particles are molecularly "soft" they decompose at lower temperatures. This is more of an issue when conducting experiments at a synchrotron however beam-caused damage can also occur using a lab based XPS system.

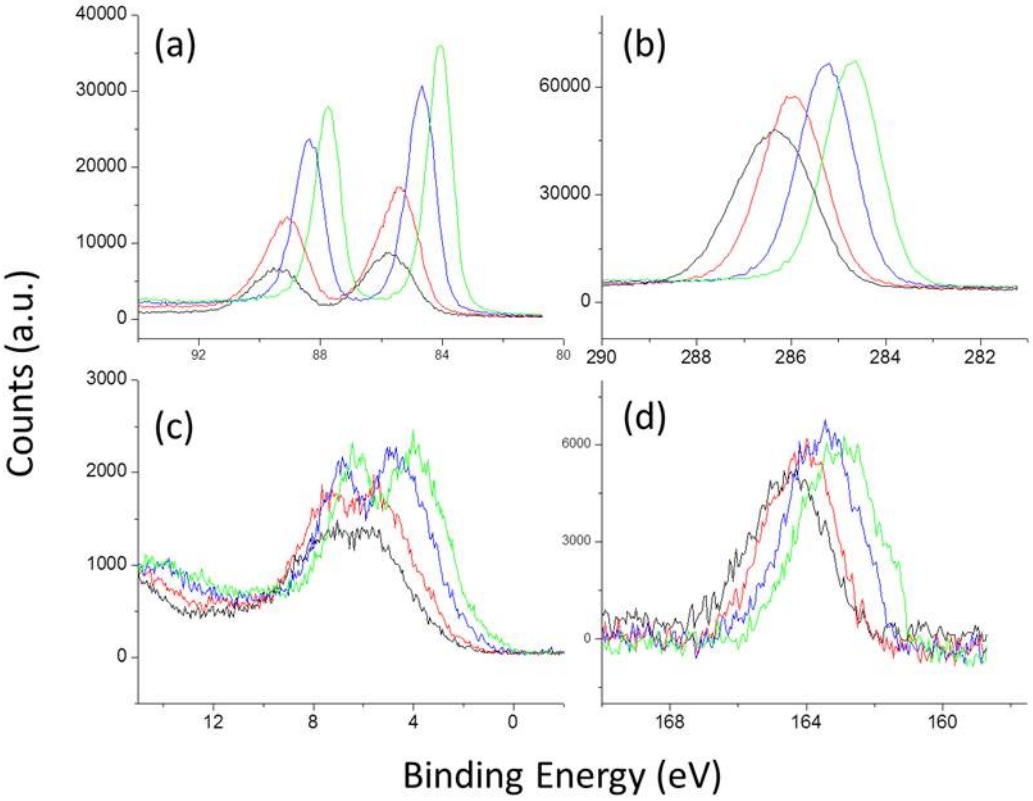

Figure A - 1: (a) Au 4f, (b) C 1s, (c) Au 5d and (d) S 2p XPS spectra for Au_{25}. Scan 1 (black) represents the initial scan while scans 2 (red), 5 (blue) and 10 (green) represent successive scans. The Au 4f peak essentially resembles that of Au foil after 10 scans.

A general shift in binding energy and change of profile for all components of Au_{25} back to that of their precursor units can be observed. This decomposition can be avoided by using a cooled sample stage. Care should also be taken during sample preparation; some nanoclusters are semi conductive and are prone to charging if layered on a sample substrate too thickly. Also, to obtain high quality valence band spectra is it best to mount

the samples on a substrate with minimal signal in the valence band region. A good choice is a Si(111) wafer (cheap and fairly conductive) however this surface is hydrophobic, thus aqueous samples do not always dry on the surface adequately. In addition some (although faint) background from the wafer does appear in the valence band region, thus blank spectra of supports should be taken when necessary.

Deconvolution of spectral features should incorporate physical restrains such as spin-orbit splitting, and degeneracy to control the position and area of the fitting components. Throughout this work constraints were applied to components of the deconvolution (i.e. peak positions, area and FWHM) whenever possible. Interestingly, it was observed that when damaged by the X-ray beam the ratio of Au:S changes with decomposition (Table B-1).

Table A-1: Area associated with each spectral feature of Au25 from XPS. The apparent ratio of Au:S increase with sample degradation. This can most likely be attributed to the changing conductivity of the Au.

Scan #	A(Au_{4f})	A(S_{2p})	A(C_{1s})	A(Au_{4f})/ A(S_{2p})
1	28219	13730	91333	2.06
2	50506	15055	91306	3.35
5	65563	18100	92300	3.62
10	67812	17700	91984	3.83

Whereas Au_{25} is a semiconductor, the reason for the apparent increase in Au concentration is likely due to the increase conductivity of bulk-like gold versus Au_{25}. This would result in an increased ability of the bulk-like Au to return to the ground state

and release a subsequent photoelectron. This result is supported by low temperature XPS results for Au_{25} which show a ratio of atomic sensitivity factors for S:Au slightly larger than what is typically observed (i.e. 0.14 vs. 0.1). This suggests that the differing electronic behavior of these clusters should be taken into account when perform quantitative analysis (i.e. stoichiometric identification) via XPS.